



Sensitivity analysis of numerical modeling input parameters on floating offshore wind turbine loads in extreme idling conditions

Will Wiley, Jason Jonkman, and Amy Robertson

National Renewable Energy Laboratory, 15013 Denver West Parkway, Golden, CO 80401, USA

Correspondence: Will Wiley (will.wiley@nrel.gov)

Received: 16 October 2024 – Discussion started: 22 October 2024

Revised: 15 January 2025 – Accepted: 7 February 2025 – Published: 19 May 2025

Abstract. Floating offshore wind turbine (FOWT) systems are subject to complex environmental loads, with significant potential for damage in extreme storm conditions. Design simulations in these conditions are required to assess the survivability of the device with some level of confidence. Aero-hydro-servo-elastic engineering tools can be used with a reasonable balance of accuracy and computational efficiency. The models require many input parameters to describe the air and water conditions, the system properties, and the load calculations. Each of these parameters has some possible range, due to either statistical uncertainty or variations with time. Variation in the input parameters can have important effects on the uncertainty in the resulting loads, but it is not practical to perform detailed assessments of the impact of this uncertainty for every input parameter. This work demonstrates a method to identify the input parameters that have the most impact on the loads to focus further inspection. The process is done specifically for extreme storm load cases defined in the International Electrotechnical Commission design requirements for floating offshore wind turbines. The analysis was performed using the International Energy Agency Wind 15 MW offshore reference wind turbine atop the University of Maine VoltturnUS-S reference platform in two US offshore wind regions, the Gulf of Maine and Humboldt Bay. It was found that the direction of incident waves and current, yaw misalignment, and the length of mooring line sections were among the primary sensitivities.

Copyright statement. This work was authored by the National Renewable Energy Laboratory, operated by the Alliance for Sustainable Energy, LLC, for the U.S. Department of Energy (DOE) under contract no. DE-AC36-08GO28308. Funding provided by U.S. Department of Energy Office of Energy Efficiency and Renewable Energy Wind Energy Technologies Office. The views expressed in the article do not necessarily represent the views of the DOE or the U.S. Government. The U.S. Government retains and the publisher, by accepting the article for publication, acknowledges that the U.S. Government retains a nonexclusive, paid-up, irrevocable, worldwide license to publish or reproduce the published form of this work, or allow others to do so, for U.S. Government purposes.

1 Introduction

Floating offshore wind turbines (FOWTs) are complex systems governed by many coupled physical effects. Numerical models of these devices are critical for understanding their performance and loads and the associated risks. Computationally efficient models are needed to optimize the design and simulate large sets of design load cases. Aero-hydro-servo-elastic time domain engineering-fidelity tools, such as OpenFAST, are commonly used for these types of simulations (NREL, 2024). These tools require a large number of input variables that describe the incident wind; aerodynamic loads; system geometry, mass/inertia, and stiffness; controller response; incident wave and current environment; and hydrodynamic loads. There are potentially thousands of variable inputs, and all of these inputs have some associated

range of variability. These ranges are an aggregate of various forms of uncertainty and changes over the life of a project. Changes to the input parameters can significantly influence the resulting ultimate and fatigue design loads. Thorough uncertainty analyses are not feasible for all input parameters but should be performed for variables that the relevant loads are most sensitive to.

An elementary effects (EE) approach has been developed and demonstrated to identify the parameters creating the largest sensitivities. Demonstrative case studies have been published that investigate incident wind parameters (Robertson et al., 2018); airfoil properties (Shaler et al., 2019); incident wind and structural property parameters (Robertson et al., 2019); wind, structure, and wake parameters for a small wind farm (Shaler et al., 2023); wind, wave, and turbine parameters for the fatigue of monopile-supported offshore turbines (Sørum et al., 2022); wind, wave, and structure parameters for a floating offshore wind turbine (Wiley et al., 2023); and wind and wave parameters for two types of floating wind turbine platforms (Reddy et al., 2024). Each of these previous studies were performed with operational load cases with mean wind speeds between cut-in and cut-out. Above-cut-out wind speeds do not occur frequently, but they can potentially cause design-driving ultimate and fatigue loads. The International Electrotechnical Commission (IEC) recognizes the importance of this possibility with the inclusion of design load case (LC) 6.1–6.5 for parked or idling turbines in the IEC 61400-3-2 floating offshore wind turbine design standard (IEC, 2024). It is also expected that the most dominant sensitivities may be different in these extreme idling conditions compared to when a turbine is operating.

A previous study of the load sensitivities of a floating offshore wind platform found very limited sensitivity to wave parameters for ultimate loads during normal operation and only secondary sensitivity to wave parameters for fatigue loads. The primary input parameter driving both types of loads was found to be the turbulence intensity of the incident wind (Wiley et al., 2023). With a nonoperational turbine in extreme conditions, it is expected that this relative significance could change.

This work uses the EE technique to identify the input parameter ranges that need the most attention when considering ultimate and fatigue loads in extreme idling conditions for a 15 MW reference floating wind system.

2 Approach

The previously developed and demonstrated EE analysis method was implemented in this work using OpenFAST to model the International Energy Agency (IEA) Wind 15 MW offshore reference wind turbine (RWT) with the University of Maine (UMaine) VoltturnUS-S reference platform.

2.1 Load cases

Four load cases were selected from the IEC floating offshore wind design requirement technical specification (IEC, 2024). There are five recommended idling load cases (LC 6.1–6.5) without fault conditions. One of these (6.2) highlights a loss of electrical network and is commonly not used by industry due to the prevalence of battery backup systems; therefore, it is not used in this work either. Three of the remaining load cases (6.1, 6.3, and 6.5) assess ultimate loads, and one of the load cases (6.4) assesses fatigue loads. The load cases are described at a high level in Table 1. The ultimate load cases feature extreme wind, wave, and current conditions with return periods of 50, 1, and 500 years, respectively. The 1-year return period of LC 6.3 also includes an extreme range of yaw misalignment. The 500-year return period of LC 6.5 is a robustness check with a safety factor of 1.0 (compared to a typical ultimate value of 1.35) and is only meant to be checked for global system survival. Fault conditions are not considered in this work.

Each of the load cases was studied for two locations: the Gulf of Maine on the US Atlantic coast and Humboldt Bay on the US Pacific coast. These two areas have the potential to be two of the first sites for floating offshore wind development in the United States. There is also publicly available metocean data near these locations. Efforts have been made to characterize these sites both for deployments and for use as academic references (Biglu et al., 2024).

2.2 System

Offshore wind turbines have continued to increase in size in recent years, with larger diameters and more flexible blades. In 2020, a team from the National Renewable Energy Laboratory (NREL), the Technical University of Denmark, and the University of Maine published the specifications for a 15 MW offshore reference turbine through IEA Wind Task 37. This turbine was designed to represent the anticipated near future of offshore turbine deployment (Gaertner et al., 2020).

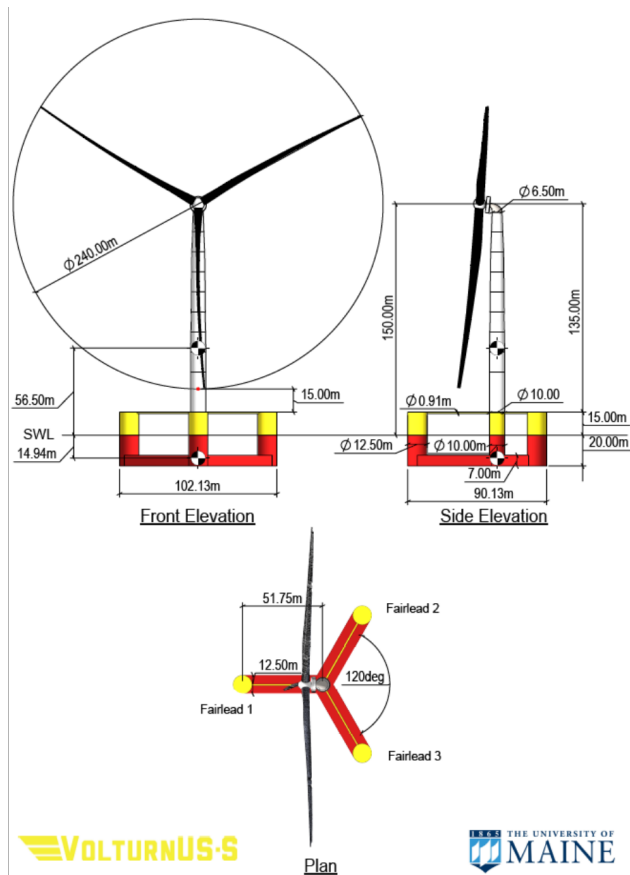
IEA Wind Task 37 also included the design of a reference floating platform to support the 15 MW turbine. The specifications of the semisubmersible UMaine VoltturnUS-S were published in 2020 by a team from the University of Maine and NREL. The design features a center-mounted tower with a three-spoke base made of fully submerged rectangular horizontal members and vertical surface-piercing cylinders (Allen et al., 2020). The reference turbine and platform are shown in Fig. 1 with some global dimensions.

2.2.1 Mooring systems

The original design of the UMaine VoltturnUS-S included a chain catenary mooring system in 200 m deep water. This water depth is within the range found in the Gulf of Maine offshore wind area but shallower than that found in the

Table 1. Selected IEC design load cases (DLCs).

IEC DLC	Wind speed	Significant wave height	Current speed	Other conditions	Load type factor	Partial safety
6.1	50 years	50 years	50 years		Ultimate	1.35
6.3	1 year	1 year	1 year	Extreme yaw misalignment	Ultimate	1.35
6.4	[cut-out, 0.7×50 years]	Joint probability distribution	Normal		Fatigue	1.00
6.5	500 years	500 years	500 years		Ultimate	1.00

**Figure 1.** UMaine VoltturnUS-S reference platform with the IEA 15 MW offshore reference wind turbine (Allen et al., 2020).

Humboldt Bay offshore wind area, which ranges between 550 and 1000 m deep (Cooperman et al., 2022). A team from NREL designed alternative reference mooring systems for this system in three locations, including the Gulf of Maine and Humboldt Bay. Both systems include sections of polyester fiber and chain. The design for the Gulf of Maine is an intermediate-depth semi-taut system, and the design for Humboldt Bay is a deep-water taut system. The systems were optimized using a quasi-static tool and verified with dynamic simulations (Lozon et al., 2025). These reference mooring designs are used in this analysis, and visualizations of the systems from the mooring specification publication are shown in Fig. 2.

2.3 Modeling

The open-source coupled aero-hydro-servo-elastic tool OpenFAST version 4.0 was used for the numerical modeling (NREL, 2024). The incident turbulent wind field was generated using TurbSim. The AeroDyn version 15 module was used for aerodynamic loads. No induction model was calculated, given the idling rotor.

Unsteady airfoil aerodynamics were not used either. In an idling condition, especially with significant angles of yaw misalignment, the angles of attack seen by the airfoils can change rapidly and with large magnitudes. Dynamic stall models are intended to capture the unsteady effects on airfoil loading due to changes in the relative inflow but are designed and tuned for angles of attack at or below stall. The deep stall potentially experienced in the load cases of this study is not well captured by existing dynamic stall models. A group from DNV demonstrated in 2023 the dependency of blade load predictions on the choice of a dynamic stall model for idling conditions. They compared predictions made with two different dynamic stall models to predictions made with steady aerodynamics using the IEA 15 MW turbine and found that loads and resulting deflections could change by an order of magnitude with a yaw misalignment of 20° . Mean values were similar in the comparison, but the amplitude of load oscillation was much larger when no dynamic stall model was used (Bangga et al., 2023). Dynamic stall models allow for the lift coefficient to temporarily exceed the steady maximum before a sharper collapse, potentially resulting in increased aerodynamic damping. Existing dynamic stall models are not able to accurately represent the large angles of attack expected to occur in this study; therefore, instead of using a correction not suited for the application, only steady airfoil aerodynamics (based on the geometric angle of attack) were used (Fuchs et al., 2023). This is the current industry standard for these load cases. Future work should be done to improve dynamic stall models for the relevant conditions; the IAG dynamic stall, for example, has been shown to predict more physically accurate loads (Bangga et al., 2023).

The air environment was modeled with the InflowWind module with turbulent inflow derived from TurbSim. A user-defined wind profile was used with a power law shear profile and linear veer profile around the value at the hub height. A Kaimal spectrum and spatial coherence model similar to

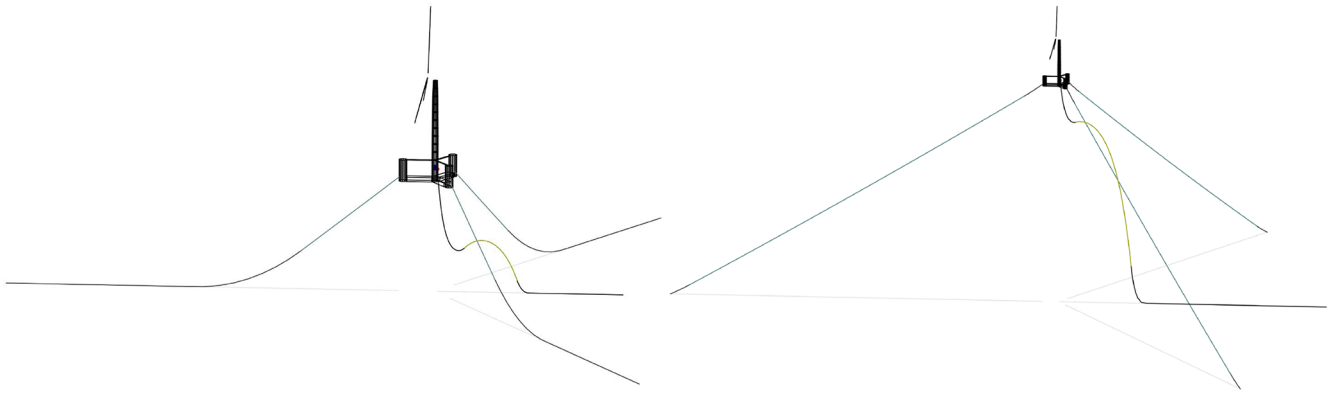


Figure 2. Mooring system visualizations for the Gulf of Maine (left) and Humboldt Bay (right) (Lozon et al., 2025).

previous analyses were used, which focus on parameters in the mean wind direction (Robertson et al., 2018).

The water environment was modeled with the SeaState module. Irregular waves were used with an embedded constrained maximum wave crest and first-order kinematics with a superimposed steady current. Vertical wave stretching was applied up to the elevation of the instantaneous free surface. The hydrodynamic forces were calculated with the HydroDyn module. The platform was represented with a hybrid model, whereby the first-order and second-order difference-frequency potential-flow coefficients were calculated using WAMIT. Strip theory transverse and axial drag coefficients were used for viscous loading.

The ElastoDyn module was used to model blade and tower deflections with predefined mode shapes. There are known inaccuracies in the reduced-order Euler–Bernoulli beam model for large deformations in flexible blades. ElastoDyn was selected over the more accurate geometrically exact beam model in the BeamDyn module due to computational cost, which will be improved through tight coupling in the upcoming OpenFAST version 5.0. The EE analysis requires a large number of simulations to be run, and the increased computational cost was not considered manageable before version 5.0 becomes available. Structural damping is also difficult to accurately capture, especially for large deflections (Chetan and Bortolotti, 2024). To avoid nonphysical blade aeroelastic instabilities at high angles of yaw misalignment, exaggerated by potentially missing aerodynamic damping from the unmodeled dynamic stall, a variable structural damping value was used for the blades. A value of 1% of critical was used when the magnitude of yaw misalignment was below 10°; above 10°, the damping linearly increased to 2% of critical at a yaw misalignment magnitude of 20°. The floating platform was treated as fully rigid to avoid high computational expense.

The mooring system was modeled using the lumped-mass-dynamics-based MoorDyn module.

Each simulation was run for 3800 s, resulting in a 1 h time series after a 200 s transient was removed. This transient pe-

riod was determined from initial simulations with nominal input parameter values.

2.4 Elementary effects

The EE method was defined by Max Morris in 1991 for general computational experiments. The technique does not identify coupling between parameters, but it reduces the total number of required simulations for a sensitivity assessment (Morris, 1991). Robertson et al. (2018) used a modification of the method that uses radial perturbations of all parameters for a sufficiently large number of starting points. This modified method has been demonstrated in previous studies and is applied to this analysis for an idling turbine in above-cut-out conditions. The approach is represented for a simplified three-parameter system in Fig. 3. The blue points represent starting points in the parameter hyperspace, and the red points are a small perturbation from the starting point in one parameter dimension only. The effect on a selected output quantity of interest (QOI) from the perturbation can be used to calculate a form of a local partial derivative scaled by the range of the parameter. Comparisons of these values calculated with different input parameter perturbations indicate the relative sensitivity to each input at that point in the hyperspace. When a sufficiently large number of starting points are used, the resulting sensitivities converge toward the global sensitivity values. In this work, the parameter hyperspace included 40 parameters.

The magnitude of the perturbations was held to a constant value of $\pm 10\%$ of the parameter range. This value has been used in previous EE analyses and aims to result in significant changes in loads without smoothing out nonlinearities (Robertson et al., 2018). The direction of the perturbation was randomly chosen with the constraint that the perturbed parameter still needed to be within the defined range. The starting point locations followed a Sobol sequence, which leads to a uniform distribution where added points evenly fill the parameter hyperspace, starting with the hyperspace midpoint (Sobol, 1967).

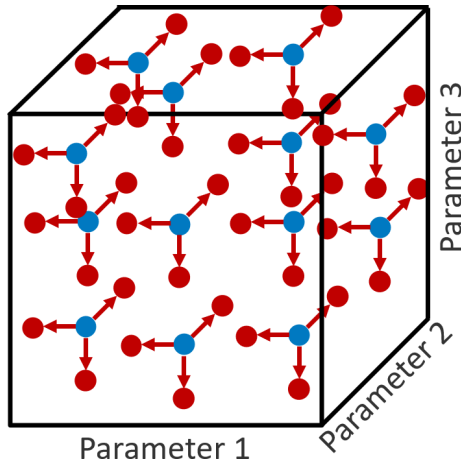


Figure 3. Three-parameter representation of input parameter hyperspace with a set of starting points shown in blue and individual parameter perturbation shown in red, adapted from Shaler et al. (2019).

Each test point was run with a number of random seed numbers used for the irregular wave and turbulent wind field generation, and the convergence of the sensitivities was tracked to ensure that a sufficient number of seed numbers was used. Both the ultimate and the fatigue loads were averaged across all seed numbers for a given set of inputs. Ultimate output loads were used for LC 6.1, 6.3, and 6.5 and were calculated following Eq. (1), where Y is an output QOI, U is a certain set of inputs, and S is the number of random seed numbers. PSF is the partial safety factor as designated by the load case in Table 1.

$$Y_{ult.}(U) = \frac{PSF}{S} \sum_{s=1}^S \text{MAX}(|Y(U)|) \tag{1}$$

Fatigue loads were used for LC 6.4 and were calculated as damage-equivalent loads (DELs) following Eq. (2). A rainflow counter was used to determine the number of cycles (n) for different amplitude oscillations of each output QOI. A constant Wöhler exponent (w) was used. The output QOI pertaining to composite components used a value of $w = 10.0$, and the QOI pertaining to steel elements used a value of $w = 4.0$. N is the number of cycles for the equivalent load, and a value of 3600 was used for a 1 Hz DEL given the 3600 s non-transient time. The value N scales all loads equally and has no effect on the final fatigue load sensitivity conclusions.

$$Y_{fat.}(U) = \frac{1}{S} \sum_{s=1}^S \left(\sum \frac{n}{N} Y(U)^w \right)^{\frac{1}{w}} \tag{2}$$

Ultimate load EE values were calculated following Eq. (3), where U^b represents the set of input parameters at some starting point, b , and x_i is a perturbation in only one input parameter, i . The EE value is normalized with the total range of

the input parameter for that load case so that the sensitivity can be compared between different input parameters. For the fixed perturbation size in this project of 10%, the change in the output QOI is effectively multiplied by 10. Ultimate load EE values include the addition of the QOI value based on all nominal values for a given load case, \overline{Y}_{LC} . This allows for the ultimate load sensitivities to be compared across multiple load cases. If a specific load case does not lead to critical ultimate loads for a specific QOI, the sensitivity is less likely to be relatively important.

$$UEE_{iLC}^b = \left| \frac{Y_{ult.}(U^b + x_i) - Y_{ult.}(U^b)}{\Delta_{iLC}} u_{iLC,range} \right| + \overline{Y}_{LC} \tag{3}$$

Fatigue load EE values were calculated in a similar way, following Eq. (4). No nominal value was added to the fatigue value, as the focus is on the variability in the loading. There is also only one load case in this study that considers fatigue loads.

$$FEE_{iLC}^b = \left| \frac{Y_{fat.}(U^b + x_i) - Y_{fat.}(U^b)}{\Delta_{iLC}} u_{iLC,range} \right| \tag{4}$$

For a given QOI, all relevant load case EE results were compared. Significant EE values were defined as those larger than a threshold of 2 standard deviations above the mean. This is shown in Eq. (5), where SEE is a significant EE value, σ is the standard deviation of EE values for a QOI, and μ is the mean EE value for a QOI.

$$SEE > 2\sigma + \mu \tag{5}$$

These significant EE values were counted, and the relative number of significant EE values coming from perturbations in a certain input parameter indicate the sensitivity to that input.

3 Input parameters

A set of 40 input parameters were selected based on expectations of possible sensitivities. These include parameters that were found to be important in previous studies and additions that were expected to be potentially relevant to above-cut-out conditions. The list of selected variables is shown in Table 2, and the corresponding labels are used in the following text and figures.

Definitions of the wind parameters are the same as in the 2018 study that focused fully on the incident wind (Robertson et al., 2018). Although veer is not defined by the IEC for the relevant load cases, it was included, as any source of asymmetry or imbalance for the idling rotor was expected to have potentially important changes to loads. Large-eddy simulations of hurricanes have shown that high veer is likely to be present in extreme conditions (Sanchez Gomez et al., 2023). Additionally, as rotor sizes increase, the impact of veer will likely grow.

Table 3. Modeling input parameter ranges and nominal values for the Gulf of Maine. Ptfm: platform, Nac: nacelle, Stat: static, Dyn: dynamic.

	6.1			6.3			6.4			6.5		
	Min	Nominal	Max									
U_{mean}	37.58	38.96	40.04	33.84	34.57	35.45	25.00	34.57	28.03	37.91	40.32	43.42
Shear	0.082	0.110	0.167	0.082	0.110	0.185	0.057	0.110	0.221	0.082	0.110	0.163
Veer	0.0000	0.0000	0.0249	0.0000	0.0000	0.0332	0.0000	0.0000	0.0616	0.0000	0.0000	0.0249
γ_{wind}	0.0	0.0	1.0	0.0	0.0	1.0	0.0	0.0	1.0	0.0	0.0	1.0
σ_u	3.546	3.701	4.013	3.146	3.284	3.561	2.413	3.284	2.731	3.669	3.830	4.153
L_u	25.0	340.2	1600.0	25.0	340.2	1600.0	25.0	340.2	1600.0	25.0	340.2	1600.0
a_u	1.5	12	26	1.5	12	26	1.5	12	26	1.5	12	26
b_u	0	0.000353	0.05	0	0.000353	0.05	0	0.000353	0.05	0	0.000353	0.05
Cl_{tip}	-0.26	0.0	0.26	-0.26	0.0	0.26	-0.26	0.0	0.26	-0.26	0.0	0.26
Cd_{tip}	-1.0	0.0	1.0	-1.0	0.0	1.0	-1.0	0.0	1.0	-1.0	0.0	1.0
Cl_{root}	-0.26	0.0	0.26	-0.26	0.0	0.26	-0.26	0.0	0.26	-0.26	0.0	0.26
Cd_{root}	-1.0	0.0	1.0	-1.0	0.0	1.0	-1.0	0.0	1.0	-1.0	0.0	1.0
$Cd_{nacelle}$	1	1.2	1.4	1	1.2	1.4	1	1.2	1.4	1	1.2	1.4
Yaw	-8	0	8	-20	0	20	-8	0	8	-8	0	8
Θ_{blade}	-2.0	0.0	2.0	-2.0	0.0	2.0	-2.0	0.0	2.0	-2.0	0.0	2.0
Twist _{tip}	-2.0	0.0	2.0	-2.0	0.0	2.0	-2.0	0.0	2.0	-2.0	0.0	2.0
TK	0.707	1	1.216	0.707	1	1.216	0.707	1	1.216	0.707	1	1.216
TD	0.1	1	5	0.1	1	5	0.1	1	5	0.1	1	5
COG _X	-1.035	0.0	1.035	-1.035	0.0	1.035	-1.035	0.0	1.035	-1.035	0.0	1.035
COG _Z	-4.8145	-4.7201	-4.6257	-4.8145	-4.7201	-4.6257	-4.8145	-4.7201	-4.6257	-4.8145	-4.7201	-4.6257
IYY	-15.1	-14.4	-13.7	-15.1	-14.4	-13.7	-15.1	-14.4	-13.7	-15.1	-14.4	-13.7
IZZ	4.1896	4.2751	4.3606	4.1896	4.2751	4.3606	4.1896	4.2751	4.3606	4.1896	4.2751	4.3606
Mass	1.23 × 10 ¹⁰	1.25 × 10 ¹⁰	1.28 × 10 ¹⁰	1.23 × 10 ¹⁰	1.25 × 10 ¹⁰	1.28 × 10 ¹⁰	1.23 × 10 ¹⁰	1.25 × 10 ¹⁰	1.28 × 10 ¹⁰	1.23 × 10 ¹⁰	1.25 × 10 ¹⁰	1.28 × 10 ¹⁰
K_{fiber}	2.32 × 10 ¹⁰	2.37 × 10 ¹⁰	2.41 × 10 ¹⁰	2.32 × 10 ¹⁰	2.37 × 10 ¹⁰	2.41 × 10 ¹⁰	2.32 × 10 ¹⁰	2.37 × 10 ¹⁰	2.41 × 10 ¹⁰	2.32 × 10 ¹⁰	2.37 × 10 ¹⁰	2.41 × 10 ¹⁰
L_{fiber}	2.38 × 10 ⁷	2.42 × 10 ⁷	2.47 × 10 ⁷	2.38 × 10 ⁷	2.42 × 10 ⁷	2.47 × 10 ⁷	2.38 × 10 ⁷	2.42 × 10 ⁷	2.47 × 10 ⁷	2.38 × 10 ⁷	2.42 × 10 ⁷	2.47 × 10 ⁷
M_{chain}	1.75 × 10 ⁷	1.78 × 10 ⁷	1.82 × 10 ⁷	1.75 × 10 ⁷	1.78 × 10 ⁷	1.82 × 10 ⁷	1.75 × 10 ⁷	1.78 × 10 ⁷	1.82 × 10 ⁷	1.75 × 10 ⁷	1.78 × 10 ⁷	1.82 × 10 ⁷
Depth	6.34 × 10 ⁵	6.47 × 10 ⁵	6.60 × 10 ⁵	6.34 × 10 ⁵	6.47 × 10 ⁵	6.60 × 10 ⁵	6.34 × 10 ⁵	6.47 × 10 ⁵	6.60 × 10 ⁵	6.34 × 10 ⁵	6.47 × 10 ⁵	6.60 × 10 ⁵
Θ_{spread}	1.39 × 10 ⁸	1.42 × 10 ⁸	1.46 × 10 ⁸	1.39 × 10 ⁸	1.42 × 10 ⁸	1.46 × 10 ⁸	1.39 × 10 ⁸	1.42 × 10 ⁸	1.46 × 10 ⁸	1.39 × 10 ⁸	1.42 × 10 ⁸	1.46 × 10 ⁸
Θ_{mis}	1.55 × 10 ⁸	1.59 × 10 ⁸	1.63 × 10 ⁸	1.55 × 10 ⁸	1.59 × 10 ⁸	1.63 × 10 ⁸	1.55 × 10 ⁸	1.59 × 10 ⁸	1.63 × 10 ⁸	1.55 × 10 ⁸	1.59 × 10 ⁸	1.63 × 10 ⁸
Hs	194.81	199.80	204.80	194.81	199.80	204.80	194.81	199.80	204.80	194.81	199.80	204.80
H_{max}	468.91	480.93	492.95	468.91	480.93	492.95	468.91	480.93	492.95	468.91	480.93	492.95
XH _{max}	197.6	200.0	202.7	197.6	200.0	202.7	198.4	201.6	201.6	197.6	200.0	202.7
TP	0	0	20	0	0	20	0	0	20	0	0	20
γ_{wave}	0.0	0.0	152.4	0.0	0.0	161.3	0.0	0.0	173.9	0.0	0.0	150.5
$V_{current}$	9.27	10.56	11.46	6.90	7.13	7.39	1.88	6.55	6.55	9.98	12.47	14.72
$\Theta_{current}$	1.75	1.86	2.15	1.75	1.86	2.15	1.75	1.86	2.15	1.75	1.86	2.15
Cd_{upper}	- $\lambda/2$	0	$\lambda/2$									
Cd_{lower}	$f(Hs)$	$f(Hs, Tp)$	$f(Hs)$									
Cd_{axial}	1	1	7	1	1	7	1	1	7	1	1	7
$Cd_{rectangular}$	0.87	1.20	1.75	0.58	0.63	0.66	0.08	0.63	0.71	0.96	1.64	3.00
	0.0	0.0	180.0	0.0	0.0	180.0	0.0	0.0	180.0	0.0	0.0	180.0
	0.4	1.3	2.0	0.4	1.3	2.0	0.4	1.3	2.0	0.4	1.3	2.0
	0.4	0.4	2.0	0.4	0.4	2.0	0.4	0.4	2.0	0.4	0.4	2.0
	0.7	8.0	10.0	0.7	8.0	10.0	0.7	8.0	10.0	0.7	8.0	10.0
	0.7	4.0	10.0	0.7	4.0	10.0	0.7	4.0	10.0	0.7	4.0	10.0

Table 4. Modeling input parameter ranges and nominal values for Humboldt Bay.

	6.1			6.3			6.4			6.5		
	Min	Nominal	Max	Min	Nominal	Max	Min	Max	Min	Nominal	Max	
U_{mean}	33.97	38.33	41.03	31.35	31.95	33.20	25.00	28.72	34.29	40.59	49.90	
Shear	0.108	0.110	0.148	0.111	0.110	0.197	0.100	0.184	0.109	0.110	0.121	
Veer	0.0000	0.0000	0.0048	0.0000	0.0000	0.0139	-0.0033	0.0222	-0.0003	0.0000	0.0039	
γ_{wind}	0.0	0.0	1.0	0.0	0.0	1.0	0.0	1.0	0.0	0.0	1.0	
σ_u	3.066	3.641	4.676	2.556	3.035	3.898	2.149	3.277	3.247	3.856	4.952	
L_u	25.000	340.200	1600.000	25.0	340.2	1600.0	25.0	1600.0	25.0	340.2	1600.0	
d_u	1.5	12	26.0	1.5	12	26	1.5	26	1.5	12	26	
b_u	0	0.000353	0.05	0	0.000353	0.05	0	0.05	0	0.000353	0.05	
Cl _{tip}	-0.26	0.0	0.26	-0.26	0.0	0.26	-0.26	0.26	-0.26	0.0	0.26	
Cd _{tip}	-1.0	0.0	1.0	-1.0	0.0	1.0	-1.0	1.0	-1.0	0.0	1.0	
Cl _{root}	-0.26	0.0	0.26	-0.26	0.0	0.26	-0.26	0.26	-0.26	0.0	0.26	
Cd _{root}	-1.0	0.0	1.0	-1.0	0.0	1.0	-1.0	1.0	-1.0	0.0	1.0	
Cd _{nacelle}	1	1.2	1.4	1	1.2	1.4	1	1.4	1	1.2	1.4	
Yaw	-8	0	8	-20	0	20	-8	8	-8	0	8	
θ _{blade}	-2.0	0.0	2.0	-2.0	0.0	2.0	-2.0	2.0	-2.0	0.0	2.0	
Twist _{tip}	-2.0	0.0	2.0	-2.0	0.0	2.0	-2.0	2.0	-2.0	0.0	2.0	
TK	0.707	1	1.216	0.707	1	1.216	0.707	1.216	0.707	1	1.216	
TD	0.1	1	5	0.1	1	5	0.1	5	0.1	1	5	
COG _x	-1.035	0.0	1.035	-1.035	0.0	1.035	-1.035	1.035	-1.035	0	1.035	
COG _z	-4.8145	-4.7201	-4.6257	-4.8145	-4.7201	-4.6257	-4.8145	-4.6257	-4.8145	-4.7201	-4.6257	
COG _z	-15.1	-14.4	-13.7	-15.1	-14.4	-13.7	-15.1	-13.7	-15.1	-14.4	-13.7	
IYY	4.1896	4.2751	4.3606	4.1896	4.2751	4.3606	4.1896	4.3606	4.1896	4.2751	4.3606	
IYZ	1.23 × 10 ¹⁰	1.25 × 10 ¹⁰	1.28 × 10 ¹⁰	1.23 × 10 ¹⁰	1.25 × 10 ¹⁰	1.28 × 10 ¹⁰	1.23 × 10 ¹⁰	1.28 × 10 ¹⁰	1.23 × 10 ¹⁰	1.25 × 10 ¹⁰	1.28 × 10 ¹⁰	
IZZ	2.32 × 10 ¹⁰	2.37 × 10 ¹⁰	2.41 × 10 ¹⁰	2.32 × 10 ¹⁰	2.37 × 10 ¹⁰	2.41 × 10 ¹⁰	2.32 × 10 ¹⁰	2.37 × 10 ¹⁰	2.32 × 10 ¹⁰	2.37 × 10 ¹⁰	2.41 × 10 ¹⁰	
Mass	23756096	24240914	24725732	2.38 × 10 ⁷	2.42 × 10 ⁷	2.47 × 10 ⁷	2.38 × 10 ⁷	2.47 × 10 ⁷	2.38 × 10 ⁷	2.42 × 10 ⁷	2.47 × 10 ⁷	
Mass	17481240	17838000	18194760	1.75 × 10 ⁷	1.78 × 10 ⁷	1.82 × 10 ⁷	1.75 × 10 ⁷	1.82 × 10 ⁷	1.75 × 10 ⁷	1.78 × 10 ⁷	1.82 × 10 ⁷	
Mass	633957.1	646895	659852.9	6.34 × 10 ⁵	6.47 × 10 ⁵	6.60 × 10 ⁵	6.34 × 10 ⁵	6.60 × 10 ⁵	6.34 × 10 ⁵	6.47 × 10 ⁵	6.60 × 10 ⁵	
K _{fiber}	1.42 × 10 ⁸	1.46 × 10 ⁸	1.49 × 10 ⁸	1.42 × 10 ⁸	1.46 × 10 ⁸	1.49 × 10 ⁸	1.42 × 10 ⁸	1.49 × 10 ⁸	1.42 × 10 ⁸	1.46 × 10 ⁸	1.49 × 10 ⁸	
K _{fiber}	1.99 × 10 ⁸	2.04 × 10 ⁸	2.09 × 10 ⁸	1.99 × 10 ⁸	2.04 × 10 ⁸	2.09 × 10 ⁸	1.99 × 10 ⁸	2.09 × 10 ⁸	1.99 × 10 ⁸	2.04 × 10 ⁸	2.09 × 10 ⁸	
L _{fiber}	1344.45	1378.92	1413.39	1344.45	1378.92	1413.39	1344.45	1413.39	1344.45	1378.92	1413.39	
M _{chain}	280.80	288.00	295.20	280.80	288.00	295.20	280.80	295.20	280.80	288.00	295.20	
Depth	797.8	800.0	802.4	797.8	800.0	802.4	797.8	801.5	797.8	800.0	802.4	
θ _{spread}	0	0	20	0	0	20	0	20	0	0	20	
θ _{mis}	0.0	0.0	171.0	0.0	0.0	177.6	0.0	168.4	0.0	0.0	170.1	
H _s	10.68	11.48	11.97	8.27	8.54	8.87	3.05	6.07	11.07	12.44	13.35	
H _{max}	1.75	1.86	2.15	1.75	1.86	2.15	1.75	2.15	1.75	1.86	2.15	
XH _{max}	-λ/2	0	λ/2	-λ/2	0	λ/2	-λ/2	λ/2	-λ/2	0	λ/2	
TP	$f(H_s)$											
Y _{wave}	1	$f(H_s, TP)$	7	1	$f(H_s, TP)$	7	1	$f(H_s)$	1	$f(H_s, TP)$	7	
Y _{wave}	0.99	1.00	1.00	0.98	0.99	0.99	0.03	0.47	0.99	1.00	1.01	
θ _{current}	0.0	0.0	180.0	0.0	0.0	180.0	0.0	180.0	0.0	0.0	180.0	
Cd _{clupper}	0.4	1.3	2.0	0.4	1.3	2.0	0.4	2.0	0.4	1.3	2.0	
Cd _{lower}	0.4	0.4	2.0	0.4	0.4	2.0	0.4	2.0	0.4	0.4	2.0	
Cd _{axial}	0.7	8.0	10.0	0.7	8.0	10.0	0.7	10.0	0.7	8.0	10.0	
Cd _{rectangular}	0.7	4.0	10.0	0.7	4.0	10.0	0.7	10.0	0.7	4.0	10.0	

dini et al., 2023). In the Gulf of Maine, 21 years of data are available, and in Humboldt Bay, 23 years of data are available.

Extreme values of the wind parameters at these locations were calculated with the generalized extreme value (GEV) distribution using a block maxima approach with a block size of 1 year. Using a block maxima reduces the number of data points to fit the distribution but takes the seasonality of the environment into consideration. The probability of an extreme event should not change from one block to another. If smaller block sizes were used, error would be introduced from the seasonality of the data; a peaks-over-threshold approach has a similar challenge. There is some uncertainty in the fit and selection of a distribution. For a given distribution, a bootstrapping approach is commonly used to quantify a confidence interval of an extreme value estimation (Vanem, 2015). This is done by recalculating the distribution with a random sample with replacement from the dataset many times. Each time the distribution is calculated, the extreme values are calculated from the sample and a distribution of extreme values is formed. If the data are very consistent or if the number of data points is very large, the distribution of extreme values is narrow. If the data are not consistent or the number of data points is small, the distribution of extreme values is wide. This approach was used for determining the range of uncertainty in the extreme values of U_{mean} . The GEV distribution was calculated with 1500 resamples. The distributions of extreme values with the relevant return periods are shown in Fig. 4. The dashed red line marks the nominal value, which is calculated using the full dataset with no resampling. The two solid lines show the 0.1 and 0.9 quantiles, which were selected as the limits of the input parameter range for U_{mean} . The range of uncertainty grows with the return period and is generally larger for Humboldt Bay than for the Gulf of Maine. The full set of yearly maximum wind speeds in the Humboldt Bay data had two data points with a larger value than the main cluster. When these years are not included in a resample, the upper tail of the GEV distribution is much shorter, resulting in a lower extreme value. This binary effect leads to a bimodal shape in the bootstrapped distribution that is more pronounced for larger return periods. This can occur because of a limited dataset or because of outliers, both resulting in a larger uncertainty in the extreme value.

The shear was also extracted from the NOW-23 dataset. The vertical wind speed distribution was fit to a power law function, and the exponent was extracted at each time step. It is expected that the amount of shear in the flow is a function of U_{mean} . The ranges were selected based on the time steps with a value of U_{mean} within the range for a given load case. Figure 5 shows a normalized histogram of shear over all recorded time and normalized histograms for the time corresponding to each load case.

The veer was extracted from the NOW-23 dataset assuming a linear fit over the elevations of the undisplaced rotor.

The range for veer was also chosen based on the time with a value of U_{mean} within the corresponding range for each load case. Figure 6 shows normalized histograms for the full dataset and each load case.

The turbulence intensity ranges, defined by the value of σ_u , are based on published local measured ranges. The data for the Gulf of Maine came from a combination of land-based and offshore lidar deployed by the University of Maine (Viselli et al., 2018). The data for Humboldt Bay came from a buoy deployed by the Pacific Northwest National Laboratory (Krishnamurthy et al., 2023). The values from both sites are published as a function of U_{mean} ; however, neither function goes to high enough values of U_{mean} to cover the load cases of this work. At both locations, the value of turbulence intensity starts to converge with increasing U_{mean} , and the ranges were taken from the maximum provided speed. The turbulence intensity range was applied to the nominal value of U_{mean} for each load case to determine the σ_u range for the load case.

No site-specific information was available to describe L_u , a_u , or b_u . Ranges matching those of the highest U_{mean} load cases from previous EE studies were used (Robertson et al., 2018, 2019; Shaler et al., 2023; Wiley et al., 2023).

The range for the aerodynamic coefficients is meant to be an aggregate of uncertainties in the steady polars and is consistent with previous EE studies focusing on operational load cases (Shaler et al., 2019).

3.1.2 System and structure

The range for yaw, the angle between the wind direction and the turbine orientation, is dictated by the IEC load cases for each of the ultimate load cases for LC 6.1 and 6.3. LC 6.3 is specifically configured to check the loads with extreme yaw; the same smaller range used in LC 6.1 is also applied to LC 6.4 and 6.5 (IEC, 2024).

The ranges for $\text{Twist}_{\text{root}}$ and $\text{Twist}_{\text{tip}}$ capture collective blade pitch error and the sensitivity to some error in twist, due to either manufacturing uncertainty, changes with time, or non-captured torsional displacement (Petroni et al., 2011).

The tower stiffness was selected to result in a $\pm 15\%$ change in tower first modal frequency. The change to the stiffness was verified with a simplified test with a clamped boundary condition using BModes. Ranges for system mass and inertia were $\pm 2\%$ of the design values. This range of uncertainty was suggested by industry experts and was applied in a previous operational EE study (Wiley et al., 2023). Mooring line ranges for the fiber sections represent an aggregate of uncertainty in the original properties and changes throughout a project lifetime due to creep. The range for K_{fiber} is $\pm 2.5\%$ of the design values, and the static and dynamic stiffnesses are changed together. The ranges for L_{fiber} and M_{chain} are also $\pm 2.5\%$. These ranges were suggested by mooring industry experts, and the changes in fiber properties

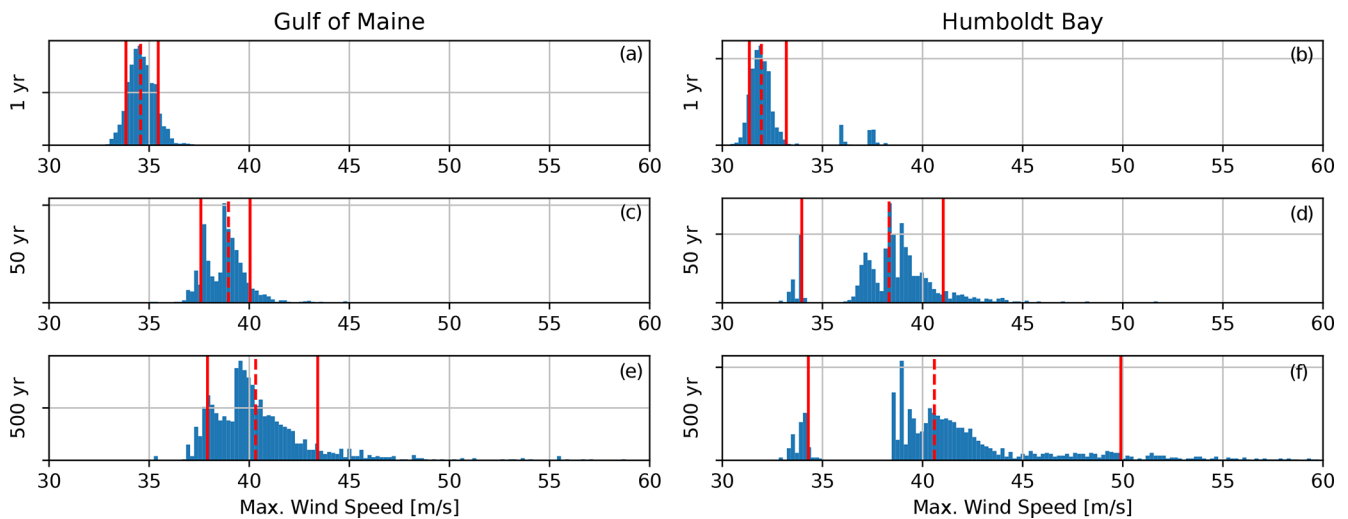


Figure 4. Bootstrapped distribution of U_{mean} with return periods of 1, 50, and 500 years based on a generalized extreme value distribution for the Gulf of Maine (a, c, e) and Humboldt Bay (b, d, f). The nominal value is based on the full dataset with no resampling and is shown with a dashed red line. The limits of the parameter range are the 0.1 and 0.9 quantiles of the bootstrapped distribution and are shown with solid red lines.

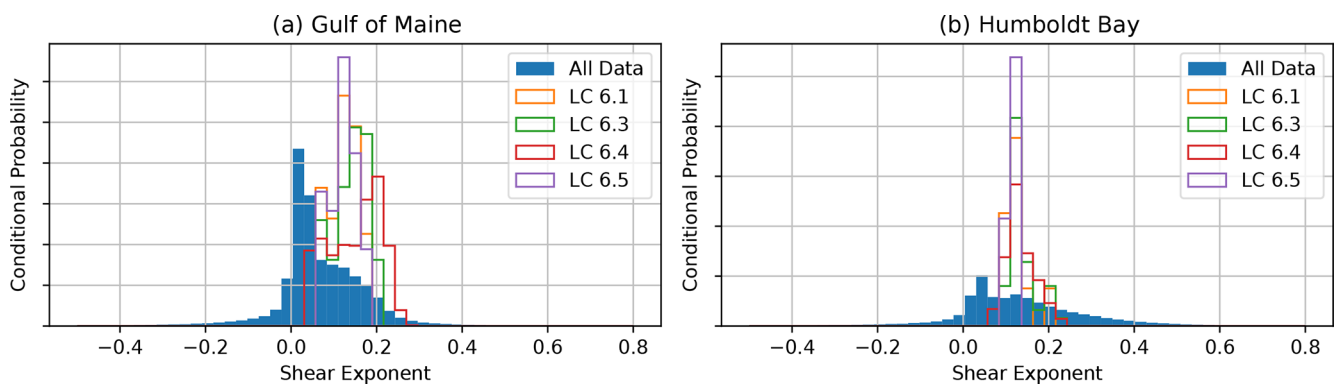


Figure 5. Shear with conditional probability based on U_{mean} ranges corresponding to IEC LC 6.1, 6.3, 6.4, and 6.5 for the Gulf of Maine (a) and Humboldt Bay (b).

through time, in particular, were highlighted as an area that needs future work.

3.1.3 Water and hydrodynamics

The ranges for depth are based on changes in time due to the water level, and the water level range is dictated by the IEC as either normal for the fatigue load cases or extreme for the ultimate load cases (IEC, 2024). Local bathymetry changes in a mooring footprint are expected to be accounted for in design and installation, while changes due to water level variation will occur in all cases. The water level range in the Gulf of Maine was described in a characterization of the site (Krieger et al., 2015). The range for Humboldt Bay was extrapolated from the ArcGIS map of tidal range (ArcGIS, 2024).

Wave data came from the National Oceanic and Atmospheric Administration's National Data Buoy Center

(NDBC). Data covering 45 years from buoy 44005 were used for the Gulf of Maine, and data covering 41 years from buoy 46022 were used for Humboldt Bay (NOAA, 2024).

No site-specific data were found to quantify the range of directional spreading, Θ_{spread} , so a maximum range of 20° was assumed. The angle between the wind direction, from the NOW-23 dataset, and the direction of the wave propagation, from the NDBC, were available to quantify Θ_{mis} . Similar to the wind shear and veer, the values of Θ_{mis} were grouped by load case based on the concurrent value of U_{mean} . The resulting normalized histograms are shown in Fig. 7. The distribution for the Humboldt Bay data is bimodal, due to a single dominant wave direction and two dominant wind directions. Even with the wind speed filtering, all load cases resulted in close to a full range of possible misalignment angles.

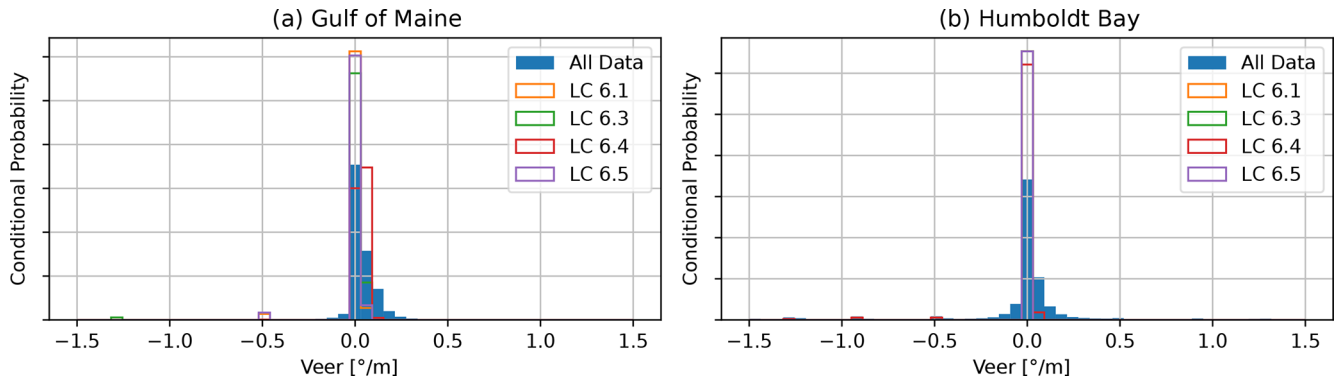


Figure 6. Veer with conditional probability based on U_{mean} ranges corresponding to IEC LC 6.1, 6.3, 6.4, and 6.5 for the Gulf of Maine (a) and Humboldt Bay (b).

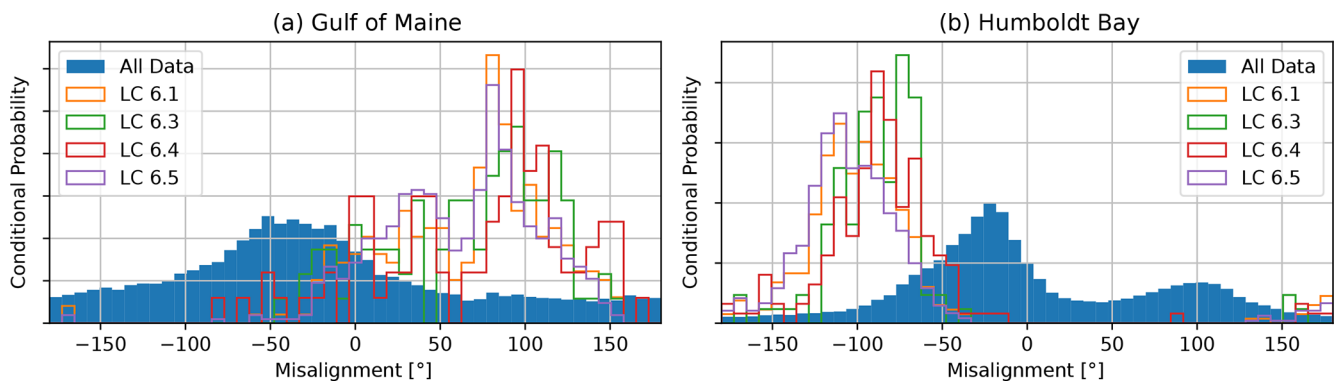


Figure 7. θ_{mis} with conditional probability based on wind speed ranges corresponding to IEC LC 6.1, 6.3, 6.4, and 6.5 for the Gulf of Maine (a) and Humboldt Bay (b).

The range of uncertainty for extreme H_s values was determined with the same GEV bootstrapping approach as the extreme U_{mean} . The resulting distributions of extreme values and the quantile ranges are shown in Fig. 8. The distribution at Humboldt Bay is narrower, resulting in a smaller range. There is a bimodal nature to the data from Humboldt Bay; this is much more apparent with larger return periods.

An embedded constrained wave of a defined maximum height is available in the SeaState module of OpenFAST. It guarantees that some maximum wave height will occur in the modeled, otherwise irregular, time series, allowing for a check of the system robustness to an extreme wave with a shorter physical time. The height, location, and the time of the embedded wave can be specified. In this study, the time was held constant but the height and location were varied. The nominal value of H_{max} comes from the IEC recommendation and is based on a value of 0.1 % exceedance with 1000 waves and a Rayleigh distribution (IEC, 2024). H_{max} is a multiplier of H_s . The limits chosen use the same 0.1 % exceedance according to a Rayleigh distribution but for a 3 h sea state with a range of average periods corresponding to expected wave periods. The position of the maximum wave

crest, XH_{max} , is a function of T_p . All possible phases of the wave were tested with a range of ± 0.5 of the wavelength.

The wave T_p was treated as a function of H_s for each combination of input parameters. The processed data from the NDBC have discrete values of T_p based on the frequency resolution used in the wave spectra. Gaussian smoothing was applied to the available wave spectra to select interpolated peaks at a higher frequency resolution. The resulting values of T_p and H_s are shown in the heat map scatter data of Fig. 9. Extreme T_p and H_s contours were generated for the relevant return periods for the ultimate load cases. The principal component analysis method within MHKit was used (Klise et al., 2020). This approach includes additional data processing prior to implementing the standard inverse first-order reliability method (I-FORM), which has been shown to better represent measured data of extreme events (Eckert-Gallup et al., 2016). The principal component analysis contours are shown in Fig. 9 for LC 6.1, 6.3, and 6.5. The H_s -dependent T_p ranges for the fatigue load case are not based on extreme value theory but mark the 0.01 and 0.99 quantiles of the NDBC data. The range of peak periods is a function of H_s selected for each run; the bounds of the range are the intersections of the relevant contour and H_s .

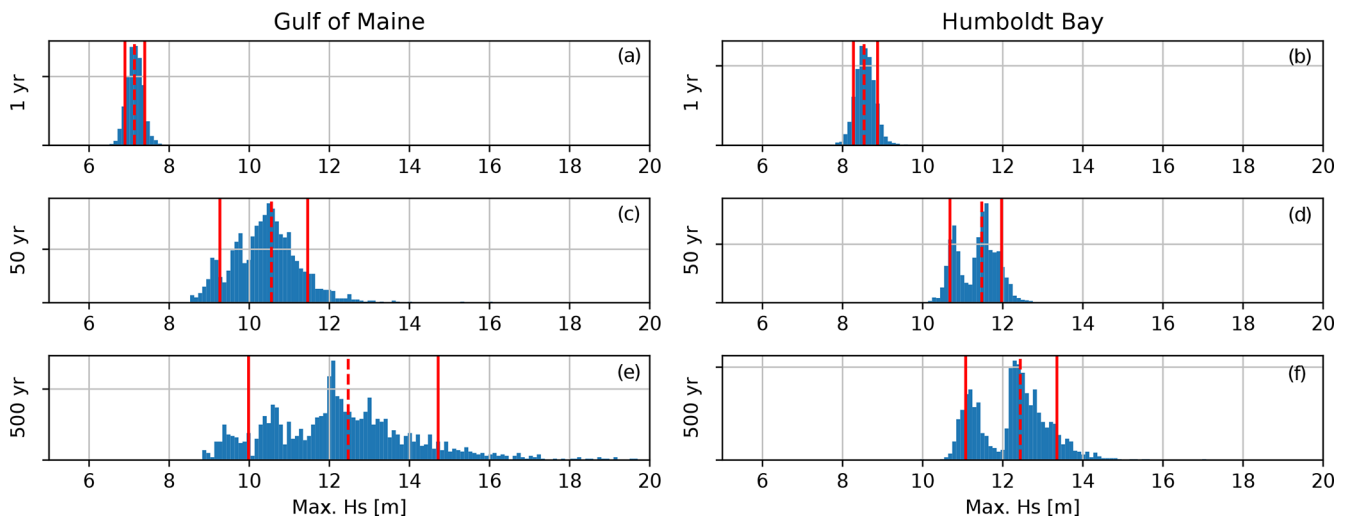


Figure 8. Bootstrapped distribution of Hs with return periods of 1, 50, and 500 years based on a generalized extreme value distribution for the Gulf of Maine (a, c, e) and Humboldt Bay (b, d, f). The nominal value is based on the full dataset with no resampling and is shown with a dashed red line. The limits of the parameter range are the 0.1 and 0.9 quantiles of the bootstrapped distribution and are shown with solid red lines.

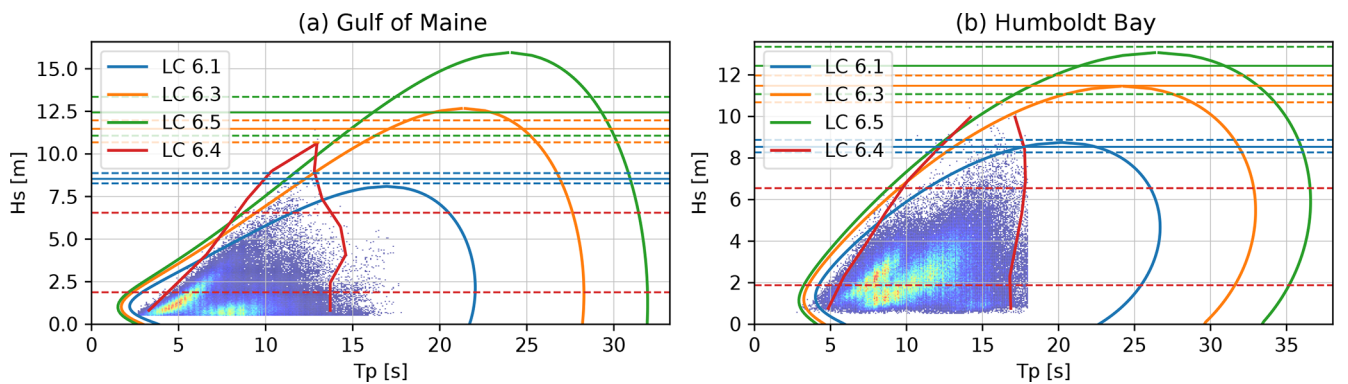


Figure 9. Tp and Hs contours with return periods of 50, 1, and 500 years corresponding to IEC LC 6.1, 6.3, and 6.5, respectively, for the Gulf of Maine (a) and Humboldt Bay (b). Extreme contours are based on the principal component analysis method, and the normal sea state contour for LC 6.4 is based on the 0.01 and 0.99 quantile of the NDBC data shown in the underlying heat map. Horizontal lines show the Hs ranges and nominal values for each load case.

The wave spectral shape factor, γ_{wave} , has a range as recommended by the American Bureau of Shipping (ABS, 2016). The nominal value is a function of Hs and Tp as specified by the IEC (IEC, 2024).

Current data also came from the NDBC; buoy 46022 was again used for Humboldt Bay, but buoy 44032 was used for the Gulf of Maine current data. The data from buoy 44032 included a full depth profile, whereas the buoy 46022 data only included one depth. At buoy 44032, a depth of 14.0 m was selected. The GEV bootstrapping method was used to determine the extreme value uncertainty ranges. The resulting distributions and limits are shown in Fig. 10. The range of speeds is much more narrow for Humboldt Bay, and the difference between values with increasing return periods is also much smaller. The distribution for the Gulf of Maine is more

positively skewed, resulting in increasingly large values with a large return period. The upper limit of the 500-year V_{current} in the Gulf of Maine was deemed unrealistic and was capped at 3.0 m s^{-1} . Current direction is allowed to range from in line with the wind direction to fully opposing.

Nominal values for the platform viscous drag coefficients came from tuning efforts to best match tank test data and computational fluid dynamics simulations for the UMaine VoltturnUS-S platform published in 2023 (Fowler et al., 2023). The ranges for the cylindrical transverse coefficients are based on the range of expected Reynolds numbers and Keulegan–Carpenter numbers. The selected ranges match those of a sensitivity study performed for this platform by a group from the Centro Nacional de Energías Renovables (CENER) and University of Stuttgart that focused specif-

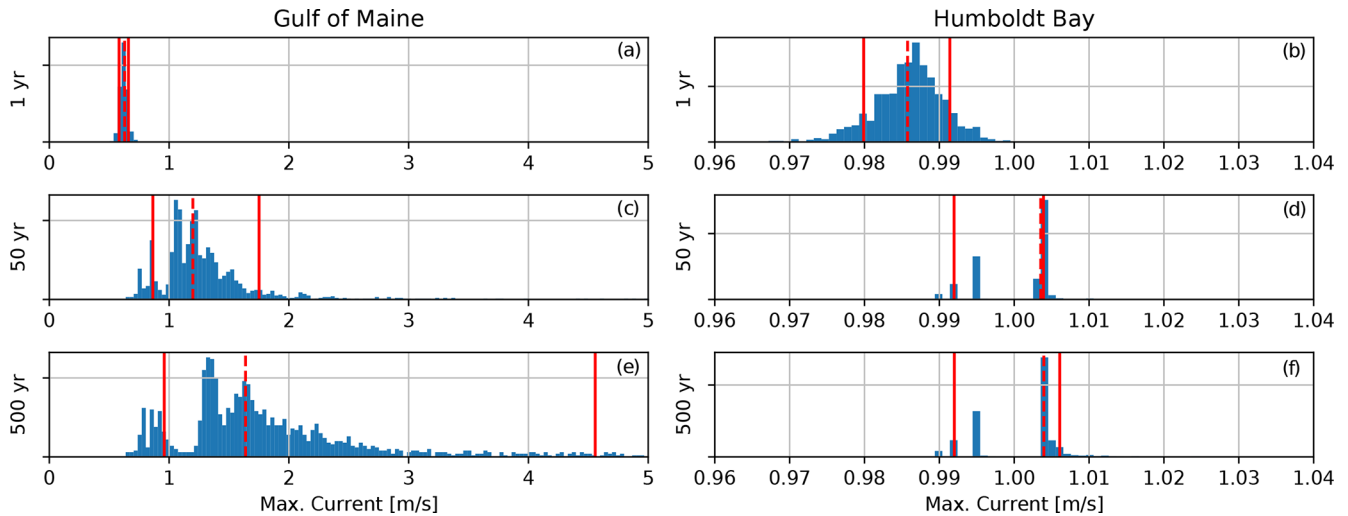


Figure 10. Bootstrapped distribution of V_{current} with return periods of 1, 50, and 500 years based on a generalized extreme value distribution for the Gulf of Maine (a, c, e) and Humboldt Bay (b, d, f). The nominal value is based on the full dataset with no resampling and is shown with a dashed red line. The limits of the parameter range are the 0.1 and 0.9 quantiles of the bootstrapped distribution and are shown with solid red lines.

ically on platform drag (Sandua-Fernandez et al., 2022). Both $C_{d_{\text{axial}}}$ and $C_{d_{\text{rectangular}}}$ have viscous drag due to separated flow around sharp corners. The ranges are based on Keulegan–Carpenter number dependence found in experiments done by a group from the University of Edinburgh, University of Strathclyde, and University of Glasgow and Fyvie with horizontally submerged rectangular cylinders (Venugopal et al., 2008).

4 Output quantities of interest

The simulated fatigue and extreme loads are evaluated for 12 QOI values as shown in Table 5. LC 6.5, with extreme environmental conditions with a return period of 500 years, is only meant to be used to evaluate the support structure, so only motion and loads in the support structure are considered. The ultimate load sensitivity of the remaining seven QOI values are only assessed for LC 6.1 and 6.3.

The blade root bending moment, yaw-bearing bending moment, tower base bending moment, low-speed (LS) shaft bending moment, and watch circle are each a composite of components in two directions. For ultimate loads, the maximum vector magnitude was selected in any direction. For fatigue loads, cycles in different directions were not considered together; instead, the vectors were divided into 12 directional bins and the bin with the highest fatigue value was used for the QOI.

Nacelle acceleration, which is also a multidirectional vector, was taken as the magnitude. Heel angle was evaluated as the inverse tangent of the vector magnitude of the tangents of pitch and roll. For both ultimate and fatigue loads, the mooring line with the largest load was used for the QOI.

5 Results

A total of 209 920 OpenFAST and 46 080 TurbSim runs were used in the following analysis. The total number comes from the product of 2 locations, 4 load cases, 32 starting points, 20 seed numbers, and (1 + 40) input perturbations for OpenFAST or (1 + 8) wind input perturbations for TurbSim. If not otherwise specified, all results include the outputs from all relevant simulations.

All simulations were postprocessed for the relevant ultimate or fatigue load EE values, and significant EE events were noted following Eq. (5). Figures A1 and A2 in Appendix A show histograms for QOI values from all ultimate LC runs and the thresholds for significance.

Figure 11 shows the number of significant ultimate load EE events for the Gulf of Maine. Each bar along the horizontal axis is one of the 40 variable input parameters. Each bar is broken and colored according to the QOI that experienced a significant change with the input perturbation. QOI bars with hash marks pertain to global system loads, while QOI bars without hash marks are rotor-specific. None of the wind input parameters has a dominant sensitivity; this dramatically differs from previous analyses with operational load cases, where σ_u was the primary sensitivity for the majority of QOI values (Wiley et al., 2023). The three inputs with the most significant EE values are all direction-based: Θ_{current} , yaw, and Θ_{mis} . V_{current} also contributes a large number of significant events. Both current parameters have a large impact on the watch circle driving fairlead and mooring loads as well. It is interesting that the direction of the waves relative to the wind, Θ_{mis} , and the relative direction of the wind to the turbine, yaw, have such an important impact but the input pa-

Table 5. Output quantities of interest and the load cases they are evaluated for.

	Ultimate only			Fatigue only
	LC 6.1	LC 6.3	LC 6.5	LC 6.4
Nacelle acceleration	X	X		X
Heel angle	X	X	X	X
Watch circle	X	X	X	X
Anchor tension	X	X	X	X
Fairlead tension	X	X	X	X
Blade tip deflection	X	X		X
Twr. base mom.	X	X	X	X
Yaw-bearing yaw mom.	X	X		X
Yaw-bearing bending mom.	X	X		X
LS shaft bending mom.	X	X		X
Root pitching mom.	X	X		X
Root bending mom.	X	X		X

rameters describing the height and period of the waves have such little impact. COG_X also has a significant impact; this appears to be largely driven by the effect on the heel angle and loads impacted by the heel angle.

Figure 12 shows the ultimate load EE sensitivities for Humboldt Bay. Similar to the results in the Gulf of Maine, Θ_{current} , Θ_{mis} , COG_X , and yaw drive large sensitivities. Different from the Gulf of Maine, V_{current} has no associated significant events. This is most likely because of the very tight distribution of current speeds in Humboldt Bay, leading to less uncertainty in the extreme values, and a smaller range. The most dominant input parameter, mostly driving global QOI like the watch circle and mooring loads, is L_{fiber} . The taut mooring system in the deeper Humboldt Bay has much longer sections of polyester in the mooring design. This indicates that installations with similar mooring designs need to have a very thorough analysis and monitoring of creep.

Figures 11 and 12 include runs from LC 6.1, 6.3, and 6.5. Figure 13 includes the same sensitivities but calculated only with each load case individually for the Gulf of Maine. The threshold for a significant event is recalculated based only on the runs from each load case. For comparison to the aggregate results, the number of significant events is normalized so that the sum for each load case is 1.0. Only the input parameters with a nonzero number of significant events are included. The most dominant input parameters are similar when considering the individual load cases but display some differences. For example, yaw is clearly the primary QOI driver for LC 6.3, which includes the extreme range of yaw. The relatively large impact of yaw masks some of the other important sensitivities in LC 6.3, including V_{current} . Yaw is still important without the extreme range check, with secondary importance for LC 6.1 with a smaller range of angles. Sensitivity to V_{current} is large for LC 6.5, where the 500-year return period has a large range. Even with a relatively large range of the 500-year H_s in LC 6.5, there is almost no significant

impact caused by the wave height, while the wave direction, Θ_{mis} , is a primary parameter for all three load cases. The size and position of the embedded H_{max} similarly have little to no significant impact.

Figure 14 shows the same individual load case results for Humboldt Bay. Again, the primary sensitivities are similar to when all load cases are used. Yaw has many fewer associated significant events when only LC 6.5 is considered. In this load case, the mooring L_{fiber} has a dominant effect.

The fatigue sensitivities are based fully on LC 6.4 and are shown in Fig. 15 for the Gulf of Maine. The fatigue loads are most strongly influenced by the waves. Θ_{mis} , H_s , and T_p contribute the most significant events. Unlike with ultimate loads, the height and period matter in addition to the direction of the waves. None of the T_p ranges overlap with the resonant periods of UMaine VoltumUS-S, but the difference in fatigue response is still significant. Veer, again pertaining to the load directionality, is the most influential incident wind parameter. This is in contrast to a previous EE sensitivity analysis of a floating wind system in operational conditions, where veer was found to be the incident wind parameter with the least influence (Wiley et al., 2023).

Figure 15 shows the fatigue results for Humboldt Bay. The same three wave parameters are still important, but the relative influence of H_s is smaller. Similar to the ultimate loads, L_{fiber} contributes many significant EE events. Not only does the length of the polyester in the taut system impact mean displacements, but also the change to the mooring stiffness has important effects on the platform oscillations. Similarly, COG_X not only causes a mean heel offset but also impacts cyclic loads.

Exact fatigue failure stress curves for each system component are not used for the load quantification described in Eq. (2). Figures C1 and C2 in Appendix C show the resulting fatigue sensitivities if the standard deviation was used as a

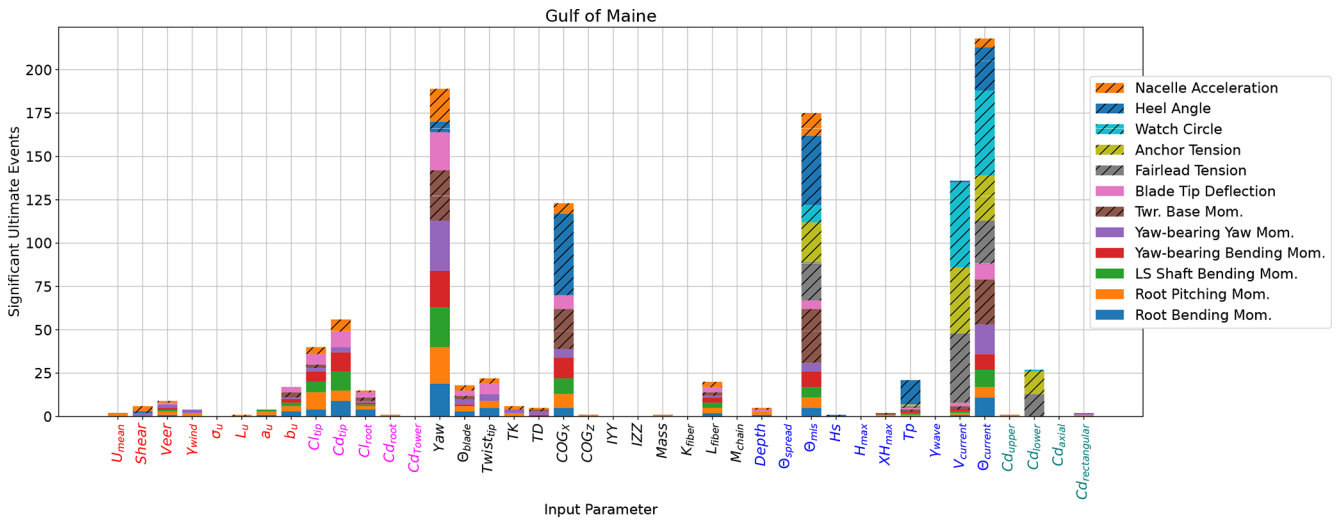


Figure 11. Sensitivity of ultimate load EE values for the IEA 15 MW RWT on the VoltturnUS-S platform in the Gulf of Maine.

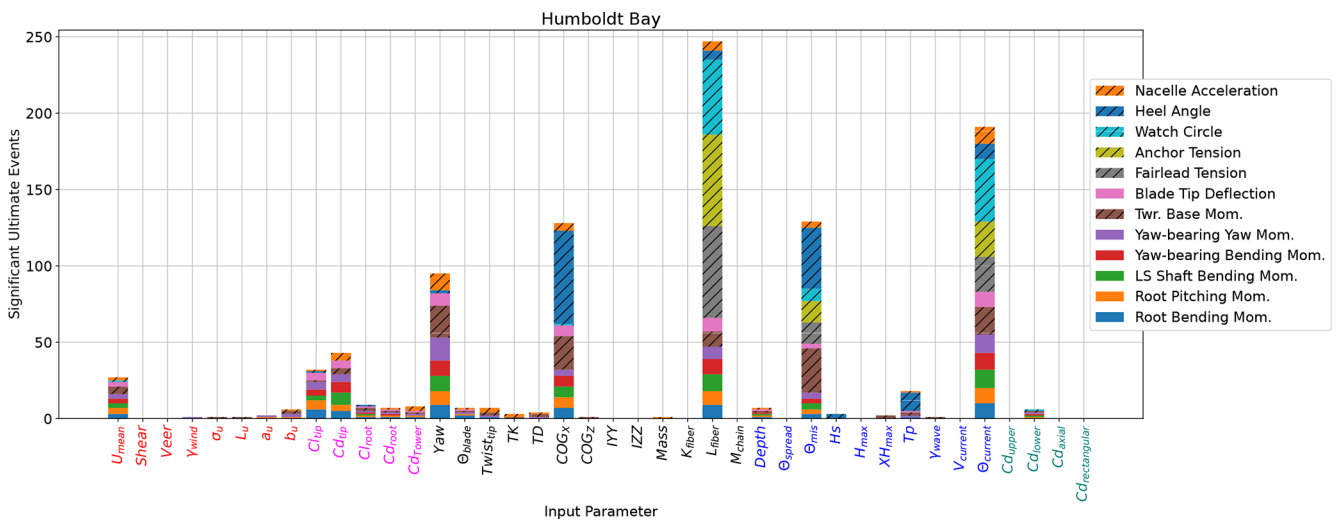


Figure 12. Sensitivity of ultimate load EE values for the IEA 15 MW RWT on the VoltturnUS-S platform in Humboldt Bay.

proxy for fatigue instead. There are no significant changes in the primary sensitivities.

Directionality appears to drive many of the idling condition loads for this floating system. Θ_{mis} is particularly interesting. The run setup in this study treats the wind direction as a constant, directly down the line of one of the mooring lines and rectangular members. Misalignment from this angle is defined by yaw for the rotor, Θ_{mis} for the waves, and $\Theta_{current}$ for the current. The input parameter definition does not make it clear whether sensitivity to Θ_{mis} is because of the relative difference between the wind and wave heading or because of the difference between the platform and wave heading. The wave loading, particularly the viscous drag effects on the rectangular members, changes depending on the relative angle of the flow and the platform.

A single additional simulation was run for the nominal starting point of LC 6.1 in the Gulf of Maine. A perturbation was made collectively to the wave heading and the wind direction as shown in the graphic in the bottom right of Fig. 17. The value of the perturbation is the same as originally tested for only the wave heading, shown in the middle graphic. Each QOI is shown for these two runs as a fraction of the QOI at the nominal starting point. If there is a deviation from the starting point with a wave-only heading change but not with a collective heading change, the impact likely comes from the misalignment of the wind and wave loading. If the deviation is similar, the impact likely comes from the differences in wave loading on the platform. It is difficult to draw conclusions from a single run comparison, but it appears that the wave orientation to the platform may be more important than or as important as the wave orientation to the wind. Sepa-

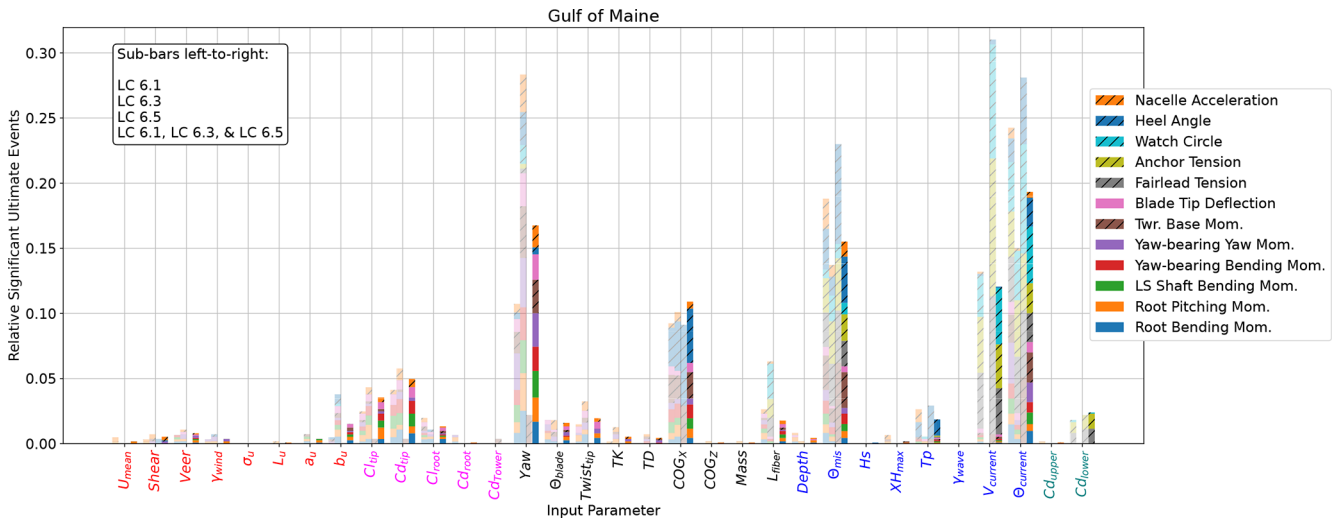


Figure 13. Sensitivity of ultimate load EE values for the IEA 15 MW RWT on the VoltturnUS-S platform in the Gulf of Maine based on IEC LC 6.1, 6.3, and 6.5 individually and on all three together. Sensitivities based on individual load cases are shown as partially transparent, and the sensitivities from the aggregate are opaque.

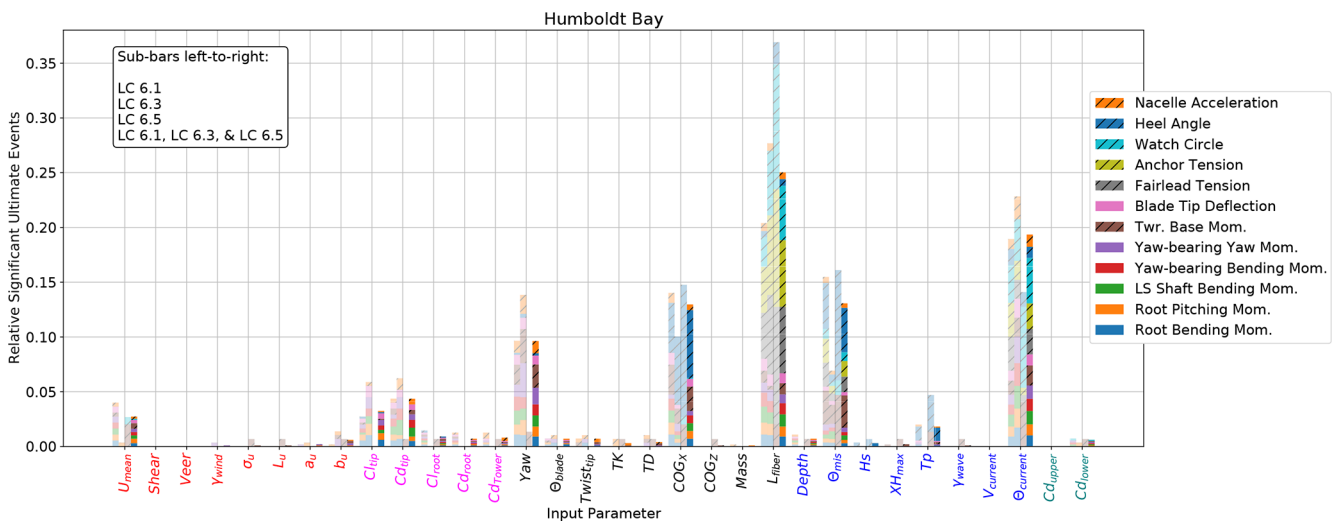


Figure 14. Sensitivity of ultimate load EE values for the IEA 15 MW RWT on the VoltturnUS-S platform in Humboldt Bay based on IEC LC 6.1, 6.3, and 6.5 individually and on all three together. Sensitivities based on individual load cases are shown as partially transparent, and the sensitivities from the aggregate are opaque.

rating the wave heading from θ_{mis} should be investigated in future work with a full investigation of the parameter hyper-space.

Tables B1, B2, B3, and B4 in Appendix B display the results for individual input parameter and QOI combination sensitivities in a detailed format. The fraction of possible runs (the total number of perturbations for a given input parameter) that exceed the significance threshold for a given QOI are shown with coloration to highlight the dominant sensitivities. A value of 1.0 would mean that all perturbations for that input parameter resulted in a significant event for that QOI.

6 Seed convergence

The turbulent wind and irregular wave fields rely on a random number generator to assign phases. The seed number can be dictated to have reproducible results and ensure unique environments if it is changed. There can be variations in loads due to differences in the seed number. For an EE sensitivity analysis, a sufficient number of seed numbers needs to be used to clearly differentiate changes due to input parameter perturbations from changes in the seed number. The QOI calculations in Eqs. (1) and (2) average across all seed numbers run for a certain set of input parameters. When enough

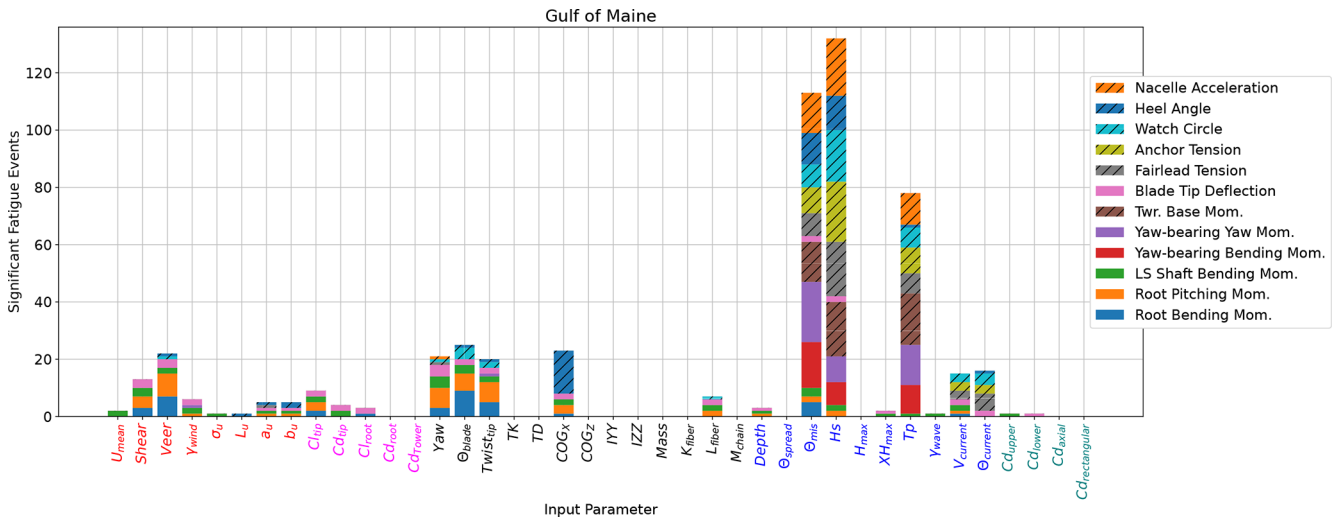


Figure 15. Sensitivity of fatigue load EE values for the IEA 15 MW RWT on the VoltturnUS-S platform in the Gulf of Maine.

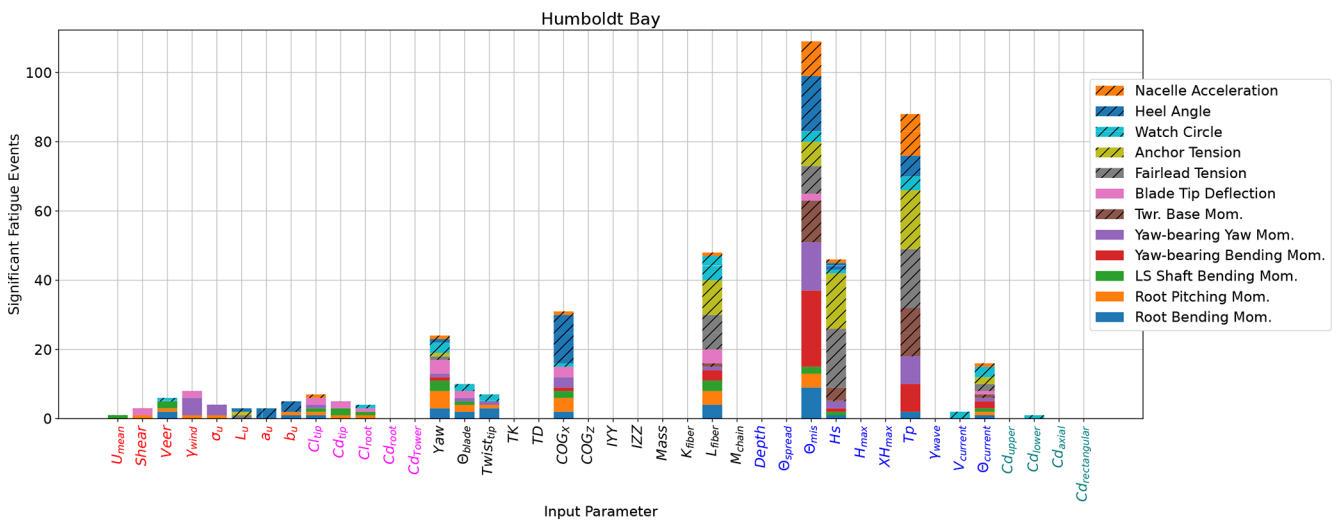


Figure 16. Sensitivity of fatigue load EE values for the IEA 15 MW RWT on the VoltturnUS-S platform in Humboldt Bay.

seed numbers are run, the results will converge so that additional seeds/runs do not result in important changes to the results.

Figures D3 and D4 show the convergence of one QOI for one starting point and one perturbation. Given the large number of input parameters, QOI, and load cases, it would be very difficult to track the convergence for each combination of input and output. Figure 18 shows how the final ultimate load EE sensitivities would look across all relevant runs if an increasing quantity of seed numbers were used, using the results from all 32 starting points. Ultimately, the relative importance of input parameters throughout the parameter hyperspace is the desired information. No changes to the primary or secondary sensitivities appear to occur after 15 seed numbers are used.

Figure 19 shows this same convergence for the fatigue load EE sensitivities. Again, the relative importance does not appear to change after 15 seed numbers are used; 20 seed numbers were used for each input parameter combination in this study.

7 Starting point convergence

The results from perturbations around each starting point provide information about the local sensitivities at that location in the parameter hyperspace. As the number of starting points increases and the aggregate results are analyzed, the resulting sensitivities approach the global sensitivity values. It is possible that at one point in the parameter hyperspace there is a very strong sensitivity to some input parameter that is not felt with other combinations of inputs. Many

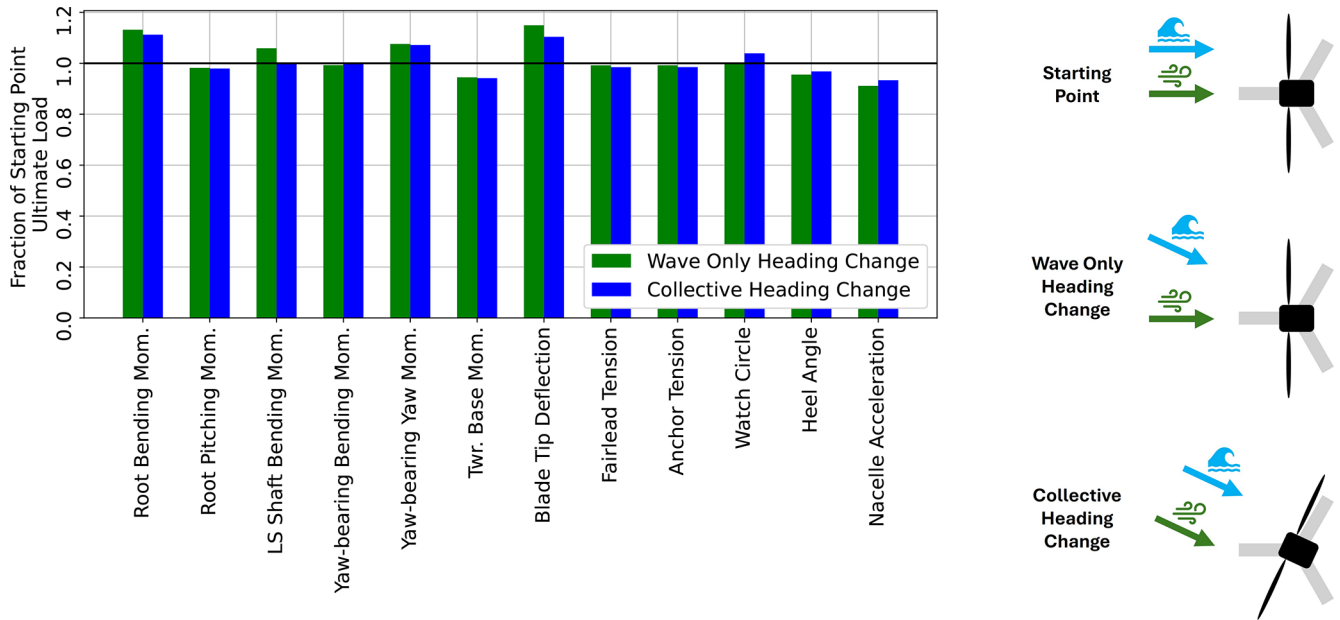


Figure 17. Changes to output loads with a perturbation in wave heading only (θ_{mis}) compared to a perturbation in collective wave heading, inflow wind angle, and nacelle yaw for the IEA 15 MW RWT on the VoltturnUS-S platform in the Gulf of Maine using nominal values for all input parameters as the starting point.

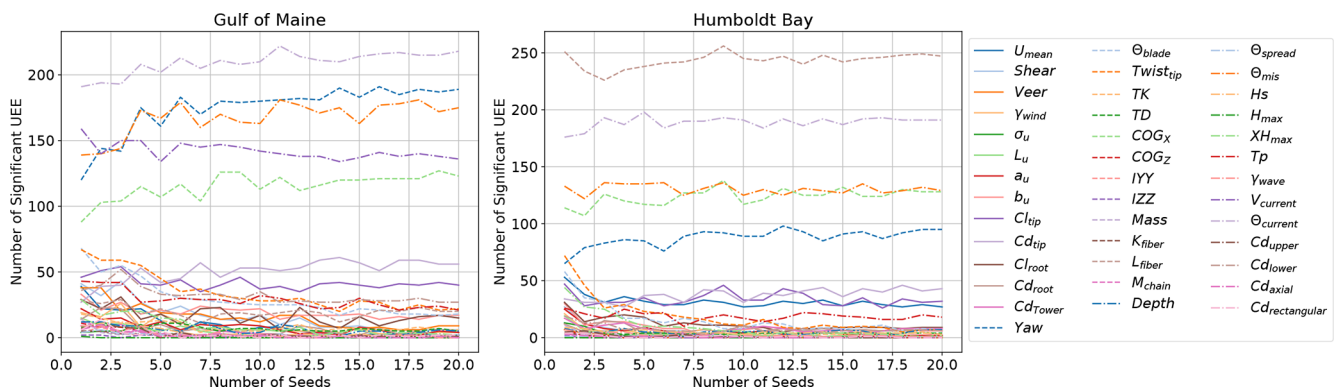


Figure 18. Convergence of ultimate load EE (UEE) sensitivity for the IEA 15 MW RWT on the VoltturnUS-S platform with an increasing number of random seed numbers.

of the input parameters have highly coupled effects, potentially leading to unique local sensitivities. To combine the impacts of these couplings across the full range of all parameters, enough starting points need to be used.

Similar to the demonstration of seed convergence, Fig. 20 shows what the final relative sensitivities would be for ultimate loads if an increasing number of starting points were used (results from all 20 seed numbers are used). This convergence is tracked with additional starting points based on the Sobol sequence, which should evenly fill the parameter hyperspace, to systematically approach the global sensitivity with as few points as possible. Note the discontinuity in the Humboldt Bay results with the addition of starting point 18. The QOI with this combination of variables happened to be

uniquely sensitive to L_{fiber} and $\Theta_{current}$, resulting in a lasting change to the relative significance. It is possible that unique coupled impacts like this occur for untested combinations of inputs; however, it appears that the identification of the dominant ultimate load EE sensitivities has converged after 30 starting points are used. A total of 32 starting points were simulated in this analysis.

Figure 21 shows the starting point convergence for the fatigue load EE sensitivity. No significant changes occur past 25 starting points.

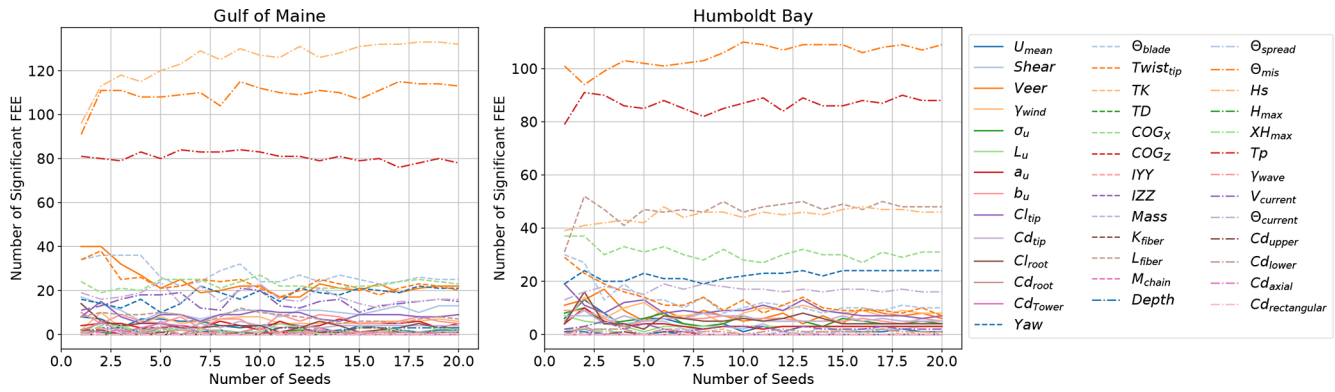


Figure 19. Convergence of fatigue load EE (FEE) sensitivity for the IEA 15 MW RWT on the VoltturnUS-S platform with an increasing number of random seed numbers.

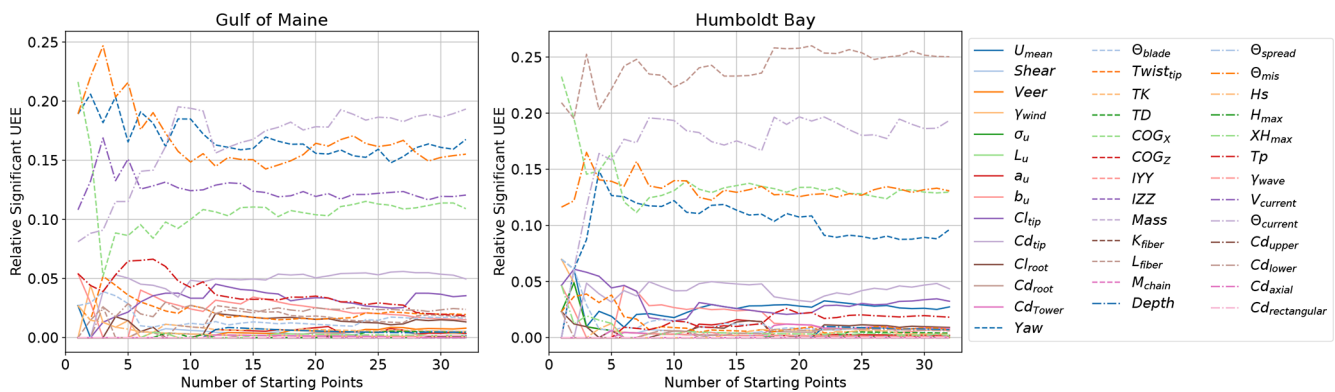


Figure 20. Convergence of ultimate load EE (UEE) sensitivity for the IEA 15 MW RWT on the VoltturnUS-S platform with an increasing number of EE starting points.

8 Conclusions

An EE approach was effectively used to identify the input parameter ranges that can have the largest impacts on ultimate and fatigue loads, specifically for above-cut-out wind conditions with an idling rotor. The dynamic stall effects and non-linear large blade deflections were not accurately captured in the efficient modeling approach used. Blade tip deflections, in particular, would likely be affected by these missing physical phenomena. Interestingly, the distribution of blade tip deflections was generally narrow enough such that a small number of significant events came from this QOI. This indicates that for the load cases studied here, uncertainties in other aspects of the numerical model, which are more accurately captured in the chosen models, are likely more important.

While wave parameters were found to have minimal impacts on the loads of an operating floating wind turbine system in previous work, the direction of waves was found to make large differences in global ultimate loads and the direction, period, and height were found to drive global fatigue loads. Incident wind input parameters had a small impact on both ultimate and fatigue loads – again, a large contrast to op-

erational load case results (Wiley et al., 2023). For extreme environmental load cases investigated in this study, more attention needs to be given to the uncertainty in wave and current parameters compared to wind parameters. This is expected due to a significant drop in the wind loading for idling conditions.

Directionality in general was shown to make large differences in the loads experienced by the IEA 15 MW UMaine VoltturnUS-S system. The orientations of the rotor, waves, and current were all primary ultimate sensitivities, and the wave direction had a strong influence on fatigue loads. There is some ambiguity as to whether the relative misalignment of the waves to the wind or the waves to the platform is more important, but it appears that both angles matter. Future studies should include the relative angle between the waves and the platform as a variable input parameter. The importance of direction could be due to a nonuniform mooring stiffness or due to differences in excitation and damping in different directions. Without the mean thrust and damping of an operating turbine, small asymmetries and misalignments can have significant impacts on loads. Changes to platform hydrody-

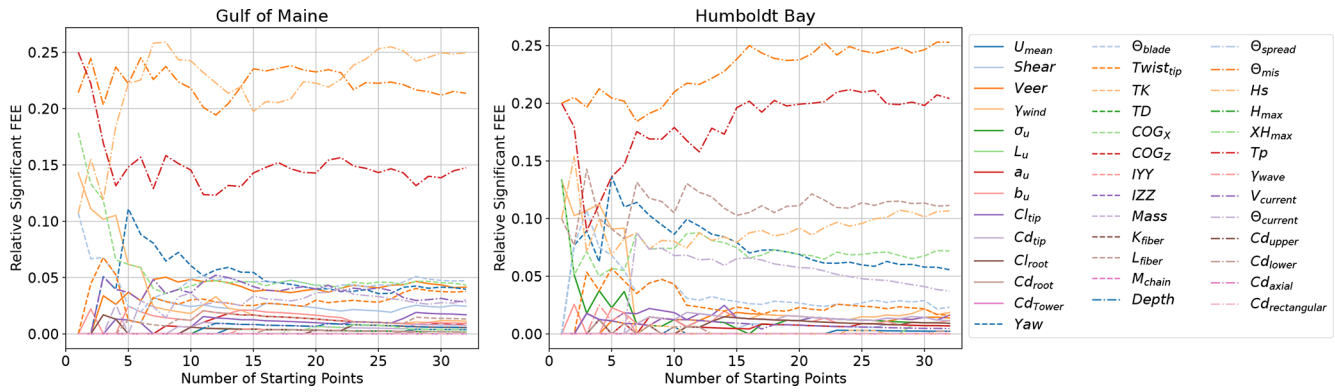


Figure 21. Convergence of fatigue load EE (FEE) sensitivity for the IEA 15 MW RWT on the VoltturnUS-S platform with an increasing number of EE starting points.

dynamic loading and mooring system properties with direction are dependent on the specific device.

Variations within the range of mooring system properties did not have dominant effects on the loads in the semi-taut moored Gulf of Maine system. However, for the taut Humboldt Bay system, with long polyester segments, L_{fiber} is very influential. As more deep-water systems are designed, focus should be placed on modeling and monitoring fiber line creep.

Appendix A: Detailed ultimate load EE values

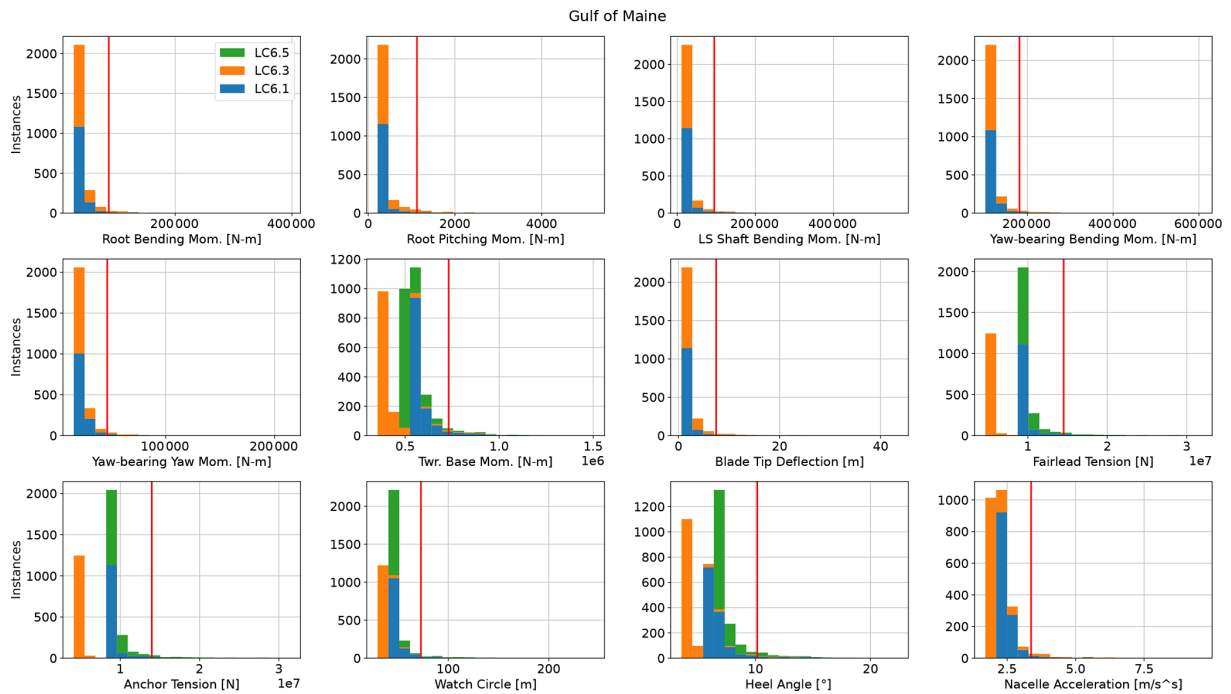


Figure A1. Histogram of ultimate load EE values for the IEA 15 MW RWT on the VoltturnUS-S platform in the Gulf of Maine for IEC LC 6.1, 6.3, and 6.5. Red line indicates 2 standard deviations above the mean, which is the threshold for a significant event.

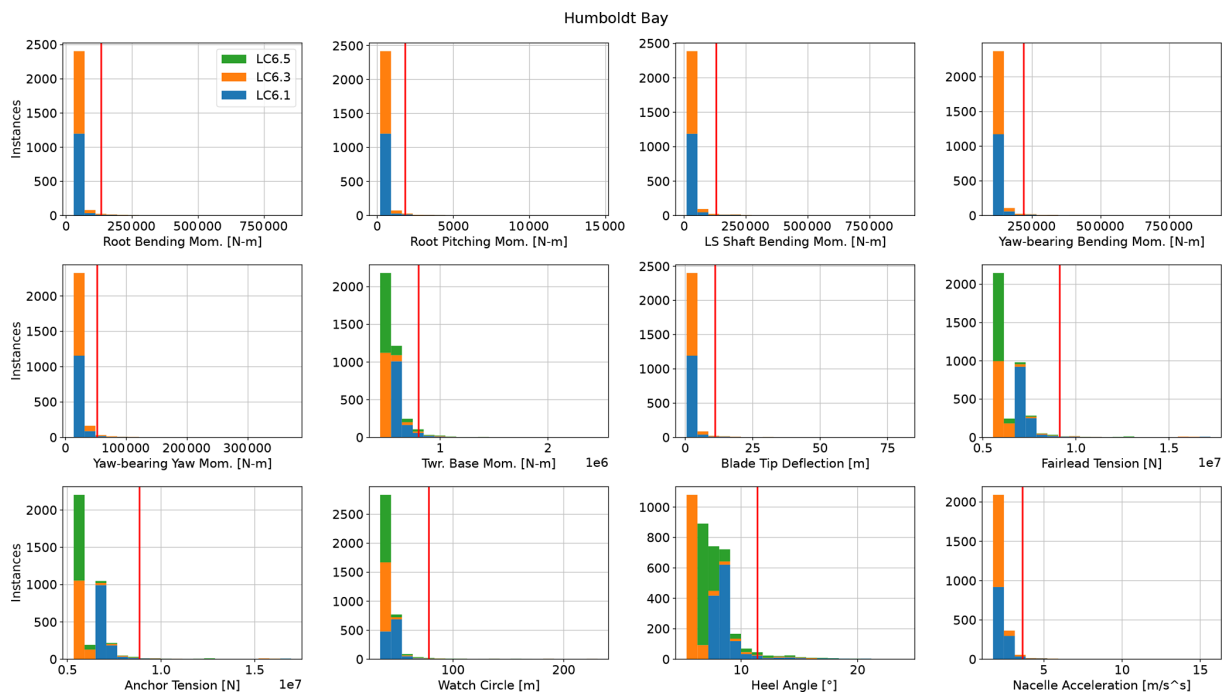


Figure A2. Histogram of ultimate load EE values for the IEA 15 MW RWT on the VoltturnUS-S platform in Humboldt Bay for IEC LC 6.1, 6.3, and 6.5. Red line indicates 2 standard deviations above the mean, which is the threshold for a significant event.

Appendix B: Sensitivity tables

Table B1. Fraction of all perturbations of a given input parameter that exceed the significant ultimate load EE threshold for a given QOI for the IEA 15 MW RWT on the VolturnUS-S platform in the Gulf of Maine.

	Root bending mom.	Root pitching mom.	LS shaft bending mom.	Yaw-bearing mom.	Yaw-bearing bending mom.	Yaw-bearing yaw mom.	Twr. base mom.	Blade tip deflection	Fairlead tension	Anchor tension	Watch circle	Heel angle	Nacelle acceleration
U_{mean}	0.00	0.03	0.00	0.00	0.00	0.00	0.00	0.00	0.00	0.00	0.00	0.00	0.00
Shear	0.00	0.00	0.00	0.00	0.03	0.00	0.00	0.00	0.00	0.00	0.01	0.05	
Veer	0.02	0.03	0.02	0.02	0.03	0.00	0.02	0.00	0.00	0.00	0.00	0.02	
Y_{wind}	0.00	0.03	0.00	0.00	0.03	0.00	0.00	0.00	0.00	0.00	0.00	0.00	
σ_u	0.00	0.00	0.00	0.00	0.00	0.00	0.00	0.00	0.00	0.00	0.00	0.00	
L_u	0.00	0.00	0.00	0.00	0.00	0.00	0.00	0.00	0.00	0.00	0.00	0.02	
a_u	0.02	0.03	0.02	0.00	0.00	0.00	0.00	0.00	0.00	0.00	0.00	0.00	
b_u	0.05	0.05	0.03	0.03	0.02	0.03	0.05	0.00	0.00	0.00	0.00	0.00	
Cl_{tip}	0.06	0.16	0.09	0.09	0.03	0.02	0.09	0.00	0.00	0.00	0.00	0.06	
Cd_{tip}	0.14	0.09	0.17	0.17	0.05	0.00	0.14	0.00	0.00	0.00	0.00	0.11	
Cl_{root}	0.06	0.03	0.02	0.02	0.02	0.02	0.05	0.00	0.00	0.00	0.00	0.02	
Cd_{root}	0.00	0.02	0.00	0.00	0.00	0.00	0.00	0.00	0.00	0.00	0.00	0.00	
Cd_{tower}	0.00	0.00	0.00	0.00	0.00	0.00	0.00	0.00	0.00	0.00	0.00	0.00	
Yaw	0.30	0.33	0.36	0.33	0.45	0.30	0.34	0.00	0.00	0.00	0.06	0.30	
Θ_{blade}	0.05	0.05	0.00	0.02	0.05	0.02	0.05	0.00	0.00	0.00	0.00	0.05	
$Twist_{tip}$	0.08	0.06	0.00	0.00	0.06	0.00	0.09	0.00	0.00	0.00	0.00	0.05	
TK	0.00	0.03	0.00	0.00	0.03	0.00	0.00	0.00	0.00	0.00	0.00	0.03	
TD	0.00	0.00	0.00	0.02	0.03	0.01	0.00	0.00	0.00	0.00	0.00	0.02	
COG_x	0.08	0.12	0.14	0.19	0.08	0.24	0.12	0.00	0.00	0.00	0.49	0.09	
COG_z	0.00	0.02	0.00	0.00	0.00	0.00	0.00	0.00	0.00	0.00	0.00	0.00	
IYY	0.00	0.00	0.00	0.00	0.00	0.00	0.00	0.00	0.00	0.00	0.00	0.00	
IZZ	0.00	0.00	0.00	0.00	0.00	0.00	0.00	0.00	0.00	0.00	0.00	0.00	
Mass	0.00	0.02	0.00	0.00	0.00	0.00	0.00	0.00	0.00	0.00	0.00	0.00	
K_{fiber}	0.00	0.00	0.00	0.00	0.00	0.00	0.00	0.00	0.00	0.00	0.00	0.00	
L_{fiber}	0.03	0.05	0.05	0.05	0.02	0.02	0.05	0.00	0.00	0.00	0.00	0.05	
M_{chain}	0.00	0.00	0.00	0.00	0.00	0.00	0.00	0.00	0.00	0.00	0.00	0.00	
Depth	0.02	0.03	0.00	0.00	0.00	0.00	0.02	0.00	0.00	0.00	0.00	0.02	
Θ_{spread}	0.00	0.00	0.00	0.00	0.00	0.00	0.00	0.00	0.00	0.00	0.00	0.00	
Θ_{mis}	0.08	0.09	0.09	0.14	0.08	0.32	0.08	0.23	0.24	0.10	0.42	0.20	
H_s	0.00	0.00	0.00	0.00	0.00	0.00	0.00	0.00	0.00	0.00	0.01	0.00	
H_{max}	0.00	0.00	0.00	0.00	0.00	0.00	0.00	0.00	0.00	0.00	0.00	0.00	
XH_{max}	0.00	0.02	0.00	0.00	0.00	0.01	0.00	0.00	0.00	0.00	0.00	0.00	
T_p	0.00	0.02	0.02	0.02	0.00	0.01	0.02	0.01	0.01	0.00	0.15	0.00	
Y_{wave}	0.00	0.00	0.00	0.00	0.00	0.00	0.00	0.00	0.00	0.00	0.00	0.00	
$V_{current}$	0.02	0.02	0.02	0.02	0.00	0.02	0.03	0.42	0.40	0.51	0.01	0.00	
$\Theta_{current}$	0.17	0.09	0.16	0.14	0.27	0.27	0.14	0.26	0.27	0.51	0.26	0.08	
Cd_{upper}	0.00	0.02	0.00	0.00	0.00	0.00	0.00	0.00	0.00	0.00	0.00	0.00	
Cd_{lower}	0.00	0.00	0.00	0.00	0.00	0.00	0.00	0.14	0.14	0.01	0.00	0.00	
Cd_{axial}	0.00	0.00	0.00	0.00	0.00	0.00	0.00	0.00	0.00	0.00	0.00	0.00	
$Cd_{rectangular}$	0.00	0.02	0.00	0.00	0.02	0.00	0.00	0.00	0.00	0.00	0.00	0.00	

Table B2. Fraction of all perturbations of a given input parameter that exceed the significant ultimate load EE threshold for a given QOI for the IEA 15 MW RWT on the VolturnUS-S platform in Humboldt Bay.

	Root bending mom.	Root pitching mom.	LS shaft bending mom.	Yaw-bearing bending mom.	Yaw-bearing bending mom.	Twr. base mom.	Blade tip deflection	Fairlead tension	Anchor tension	Watch circle	Heel angle	Nacelle acceleration
U_{mean}	0.05	0.06	0.05	0.05	0.05	0.05	0.05	0.00	0.00	0.01	0.00	0.03
<i>Shear</i>	0.00	0.00	0.00	0.00	0.00	0.00	0.00	0.00	0.00	0.00	0.00	0.00
<i>Veer</i>	0.00	0.00	0.00	0.00	0.00	0.00	0.00	0.00	0.00	0.00	0.00	0.00
Y_{wind}	0.00	0.00	0.00	0.00	0.02	0.00	0.00	0.00	0.00	0.00	0.00	0.00
σ_u	0.00	0.00	0.00	0.00	0.00	0.01	0.00	0.00	0.00	0.00	0.00	0.00
L_u	0.00	0.00	0.00	0.00	0.00	0.01	0.00	0.00	0.00	0.00	0.00	0.00
a_u	0.00	0.02	0.00	0.00	0.02	0.00	0.00	0.00	0.00	0.00	0.00	0.00
b_u	0.00	0.02	0.00	0.00	0.03	0.02	0.00	0.00	0.00	0.00	0.00	0.02
Cl_{tip}	0.09	0.09	0.05	0.06	0.08	0.01	0.08	0.00	0.00	0.00	0.01	0.02
Cd_{tip}	0.08	0.06	0.12	0.11	0.08	0.04	0.08	0.00	0.00	0.00	0.00	0.08
Cl_{root}	0.02	0.02	0.02	0.02	0.02	0.02	0.02	0.00	0.00	0.00	0.01	0.00
Cd_{root}	0.02	0.02	0.00	0.02	0.02	0.01	0.02	0.00	0.00	0.00	0.00	0.02
Cd_{tower}	0.02	0.02	0.00	0.00	0.02	0.01	0.02	0.00	0.00	0.00	0.00	0.05
<i>Yaw</i>	0.14	0.14	0.16	0.16	0.23	0.22	0.12	0.00	0.00	0.00	0.02	0.17
Θ_{blade}	0.03	0.02	0.00	0.00	0.02	0.01	0.02	0.00	0.00	0.00	0.00	0.02
$Twist_{tip}$	0.02	0.00	0.00	0.00	0.02	0.02	0.00	0.00	0.00	0.00	0.00	0.05
<i>TK</i>	0.00	0.00	0.00	0.00	0.00	0.01	0.00	0.00	0.00	0.00	0.00	0.03
<i>TD</i>	0.00	0.00	0.00	0.00	0.02	0.02	0.00	0.00	0.00	0.00	0.00	0.02
COG_x	0.11	0.11	0.11	0.11	0.06	0.23	0.11	0.00	0.00	0.01	0.64	0.08
COG_z	0.00	0.00	0.00	0.00	0.00	0.01	0.00	0.00	0.00	0.00	0.00	0.00
I_{YY}	0.00	0.00	0.00	0.00	0.00	0.00	0.00	0.00	0.00	0.00	0.00	0.00
I_{ZZ}	0.00	0.00	0.00	0.00	0.00	0.00	0.00	0.00	0.00	0.00	0.00	0.00
<i>Mass</i>	0.00	0.00	0.00	0.00	0.00	0.00	0.00	0.00	0.00	0.00	0.00	0.02
K_{fiber}	0.00	0.00	0.00	0.00	0.00	0.00	0.00	0.00	0.00	0.00	0.00	0.00
L_{fiber}	0.14	0.14	0.17	0.16	0.12	0.10	0.14	0.62	0.62	0.51	0.06	0.09
M_{chain}	0.00	0.00	0.00	0.00	0.00	0.00	0.00	0.00	0.00	0.00	0.00	0.00
<i>Depth</i>	0.02	0.02	0.02	0.02	0.00	0.01	0.02	0.00	0.00	0.00	0.00	0.02
Θ_{spread}	0.00	0.00	0.00	0.00	0.00	0.00	0.00	0.00	0.00	0.00	0.00	0.00
Θ_{mis}	0.05	0.05	0.06	0.05	0.06	0.30	0.05	0.15	0.15	0.08	0.42	0.06
H_s	0.00	0.00	0.00	0.00	0.00	0.00	0.00	0.00	0.00	0.00	0.03	0.00
H_{max}	0.00	0.00	0.00	0.00	0.00	0.00	0.00	0.00	0.00	0.00	0.00	0.00
XH_{max}	0.00	0.00	0.00	0.00	0.00	0.02	0.00	0.00	0.00	0.00	0.00	0.00
T_p	0.02	0.00	0.00	0.00	0.02	0.02	0.02	0.00	0.00	0.00	0.12	0.02
Y_{wave}	0.00	0.00	0.00	0.00	0.00	0.01	0.00	0.00	0.00	0.00	0.00	0.00
$V_{current}$	0.00	0.00	0.00	0.00	0.00	0.00	0.00	0.00	0.00	0.00	0.00	0.00
$\Theta_{current}$	0.16	0.16	0.19	0.17	0.19	0.19	0.16	0.24	0.24	0.43	0.10	0.17
Cd_{upper}	0.00	0.00	0.00	0.00	0.00	0.00	0.00	0.00	0.00	0.00	0.00	0.00
Cd_{lower}	0.00	0.02	0.02	0.02	0.02	0.01	0.00	0.00	0.00	0.01	0.00	0.00
Cd_{axial}	0.00	0.00	0.00	0.00	0.00	0.00	0.00	0.00	0.00	0.00	0.00	0.00
$Cd_{rectangular}$	0.00	0.00	0.00	0.00	0.00	0.00	0.00	0.00	0.00	0.00	0.00	0.00

Table B3. Fraction of all perturbations of a given input parameter that exceed the significant fatigue load EE threshold for a given QOI for the IEA 15 MW RWT on the VoltturnUS-S platform in the Gulf of Maine.

	Root bending mom.	Root pitching mom.	LS shaft bending mom.	Yaw-bearing bending mom.	Yaw-bearing bending mom.	Twr. base mom.	Blade tip deflection	Fairlead tension	Anchor tension	Watch circle	Heel angle	Nacelle acceleration
U_{mean}	0.00	0.00	0.06	0.00	0.00	0.00	0.00	0.00	0.00	0.00	0.00	0.00
Shear	0.09	0.12	0.09	0.00	0.00	0.00	0.09	0.00	0.00	0.00	0.00	0.00
Veer	0.22	0.25	0.06	0.00	0.00	0.00	0.09	0.00	0.00	0.03	0.03	0.00
Y_{wind}	0.00	0.03	0.06	0.00	0.03	0.00	0.06	0.00	0.00	0.00	0.00	0.00
σ_u	0.00	0.00	0.03	0.00	0.00	0.00	0.00	0.00	0.00	0.00	0.00	0.00
L_u	0.00	0.00	0.00	0.00	0.00	0.00	0.00	0.00	0.00	0.00	0.03	0.00
a_u	0.00	0.03	0.03	0.00	0.00	0.00	0.03	0.03	0.00	0.00	0.03	0.00
b_u	0.00	0.03	0.03	0.00	0.00	0.00	0.03	0.00	0.00	0.00	0.06	0.00
$C_{l_{tip}}$	0.06	0.09	0.06	0.00	0.00	0.00	0.06	0.00	0.00	0.00	0.00	0.00
$C_{d_{tip}}$	0.00	0.00	0.06	0.00	0.00	0.00	0.06	0.00	0.00	0.00	0.00	0.00
$C_{l_{root}}$	0.03	0.00	0.00	0.00	0.00	0.00	0.06	0.00	0.00	0.00	0.00	0.00
$C_{d_{root}}$	0.00	0.00	0.00	0.00	0.00	0.00	0.00	0.00	0.00	0.00	0.00	0.00
$C_{d_{tower}}$	0.00	0.00	0.00	0.00	0.00	0.00	0.00	0.00	0.00	0.00	0.00	0.00
Yaw	0.09	0.22	0.12	0.00	0.00	0.00	0.12	0.03	0.00	0.03	0.00	0.03
Θ_{blade}	0.28	0.19	0.09	0.00	0.00	0.00	0.06	0.00	0.00	0.12	0.03	0.00
$Twist_{tip}$	0.16	0.22	0.06	0.00	0.03	0.00	0.06	0.00	0.00	0.06	0.03	0.00
TK	0.00	0.00	0.00	0.00	0.00	0.00	0.00	0.00	0.00	0.00	0.00	0.00
TD	0.00	0.00	0.00	0.00	0.00	0.00	0.00	0.00	0.00	0.00	0.00	0.00
COG_x	0.03	0.09	0.06	0.00	0.00	0.00	0.06	0.00	0.00	0.00	0.47	0.00
COG_z	0.00	0.00	0.00	0.00	0.00	0.00	0.00	0.00	0.00	0.00	0.00	0.00
IYY	0.00	0.00	0.00	0.00	0.00	0.00	0.00	0.00	0.00	0.00	0.00	0.00
IZZ	0.00	0.00	0.00	0.00	0.00	0.00	0.00	0.00	0.00	0.00	0.00	0.00
Mass	0.00	0.00	0.00	0.00	0.00	0.00	0.00	0.00	0.00	0.00	0.00	0.00
K_{fiber}	0.00	0.00	0.00	0.00	0.00	0.00	0.00	0.00	0.00	0.00	0.00	0.00
L_{fiber}	0.00	0.06	0.06	0.00	0.00	0.00	0.06	0.00	0.00	0.03	0.00	0.00
M_{chain}	0.00	0.00	0.00	0.00	0.00	0.00	0.00	0.00	0.00	0.00	0.00	0.00
Depth	0.00	0.03	0.03	0.00	0.00	0.00	0.03	0.00	0.00	0.00	0.00	0.00
Θ_{spread}	0.00	0.00	0.00	0.00	0.00	0.00	0.00	0.00	0.00	0.00	0.00	0.00
Θ_{mis}	0.16	0.06	0.09	0.50	0.66	0.44	0.06	0.25	0.28	0.25	0.34	0.44
H_s	0.00	0.06	0.06	0.25	0.28	0.59	0.06	0.59	0.66	0.56	0.38	0.62
H_{max}	0.00	0.00	0.00	0.00	0.00	0.00	0.00	0.00	0.00	0.00	0.00	0.00
XH_{max}	0.00	0.00	0.03	0.00	0.00	0.00	0.03	0.00	0.00	0.00	0.00	0.00
T_p	0.00	0.00	0.03	0.31	0.44	0.56	0.00	0.22	0.28	0.22	0.03	0.34
Y_{wave}	0.00	0.00	0.03	0.00	0.00	0.00	0.00	0.00	0.00	0.00	0.00	0.00
$V_{current}$	0.03	0.03	0.06	0.00	0.00	0.00	0.06	0.09	0.09	0.09	0.00	0.00
$\Theta_{current}$	0.00	0.00	0.00	0.00	0.00	0.00	0.06	0.19	0.09	0.12	0.03	0.00
$C_{d_{upper}}$	0.00	0.00	0.03	0.00	0.00	0.00	0.00	0.00	0.00	0.00	0.00	0.00
$C_{d_{lower}}$	0.00	0.00	0.00	0.00	0.00	0.00	0.03	0.00	0.00	0.00	0.00	0.00
$C_{d_{axial}}$	0.00	0.00	0.00	0.00	0.00	0.00	0.00	0.00	0.00	0.00	0.00	0.00
$C_{d_{rectangular}}$	0.00	0.00	0.00	0.00	0.00	0.00	0.00	0.00	0.00	0.00	0.00	0.00

Table B4. Fraction of all perturbations of a given input parameter that exceed the significant fatigue load EE threshold for a given QOI for the IEA 15 MW RWT on the VolturnUS-S platform in Humboldt Bay.

	Root bending mom.	Root pitching mom.	LS shaft bending mom.	Yaw-bearing mom.	Yaw-bearing bending mom.	Yaw-bearing yaw mom.	Twr. base mom.	Blade tip deflection	Fairlead tension	Anchor tension	Watch circle	Heel angle	Nacelle acceleration
U_{mean}	0.00	0.00	0.03	0.00	0.00	0.00	0.00	0.00	0.00	0.00	0.00	0.00	0.00
Shear	0.00	0.03	0.00	0.00	0.00	0.00	0.06	0.00	0.00	0.00	0.00	0.00	0.00
Veer	0.06	0.03	0.06	0.00	0.00	0.00	0.00	0.00	0.00	0.03	0.00	0.00	0.00
Y_{wind}	0.00	0.03	0.00	0.00	0.16	0.00	0.06	0.00	0.00	0.00	0.00	0.00	0.00
σ_u	0.00	0.03	0.00	0.00	0.09	0.00	0.00	0.00	0.00	0.00	0.00	0.00	0.00
L_u	0.00	0.00	0.00	0.00	0.00	0.00	0.00	0.03	0.03	0.00	0.03	0.00	0.00
a_u	0.00	0.00	0.00	0.00	0.00	0.00	0.00	0.00	0.00	0.00	0.09	0.00	0.00
b_u	0.03	0.03	0.00	0.00	0.00	0.00	0.00	0.00	0.00	0.00	0.09	0.00	0.00
Cl_{tip}	0.03	0.03	0.03	0.00	0.03	0.00	0.06	0.00	0.00	0.00	0.00	0.03	0.00
Cd_{tip}	0.00	0.03	0.06	0.00	0.00	0.00	0.06	0.00	0.00	0.00	0.00	0.00	0.00
Cl_{root}	0.00	0.03	0.03	0.00	0.00	0.00	0.03	0.00	0.00	0.03	0.00	0.00	0.00
Cd_{root}	0.00	0.00	0.00	0.00	0.00	0.00	0.00	0.00	0.00	0.00	0.00	0.00	0.00
Cd_{tower}	0.00	0.00	0.00	0.00	0.00	0.00	0.00	0.00	0.00	0.00	0.00	0.00	0.00
Yaw	0.09	0.16	0.09	0.03	0.03	0.00	0.12	0.03	0.03	0.09	0.03	0.03	0.03
Θ_{blade}	0.06	0.06	0.03	0.00	0.03	0.00	0.06	0.00	0.00	0.06	0.00	0.00	0.00
$Twist_{tip}$	0.09	0.03	0.00	0.00	0.03	0.00	0.00	0.00	0.00	0.06	0.00	0.00	0.00
TK	0.00	0.00	0.00	0.00	0.00	0.00	0.00	0.00	0.00	0.00	0.00	0.00	0.00
TD	0.00	0.00	0.00	0.00	0.00	0.00	0.00	0.00	0.00	0.00	0.00	0.00	0.00
COG_x	0.06	0.12	0.06	0.03	0.09	0.00	0.09	0.00	0.00	0.03	0.44	0.03	0.03
COG_z	0.00	0.00	0.00	0.00	0.00	0.00	0.00	0.00	0.00	0.00	0.00	0.00	0.00
IYY	0.00	0.00	0.00	0.00	0.00	0.00	0.00	0.00	0.00	0.00	0.00	0.00	0.00
IZZ	0.00	0.00	0.00	0.00	0.00	0.00	0.00	0.00	0.00	0.00	0.00	0.00	0.00
Mass	0.00	0.00	0.00	0.00	0.00	0.00	0.00	0.00	0.00	0.00	0.00	0.00	0.00
K_{fiber}	0.00	0.00	0.00	0.00	0.00	0.00	0.00	0.00	0.00	0.00	0.00	0.00	0.00
L_{fiber}	0.12	0.12	0.09	0.09	0.03	0.03	0.12	0.31	0.31	0.22	0.00	0.03	0.03
M_{chain}	0.00	0.00	0.00	0.00	0.00	0.00	0.00	0.00	0.00	0.00	0.00	0.00	0.00
Depth	0.00	0.00	0.00	0.00	0.00	0.00	0.00	0.00	0.00	0.00	0.00	0.00	0.00
Θ_{spread}	0.00	0.00	0.00	0.00	0.00	0.00	0.00	0.00	0.00	0.00	0.00	0.00	0.00
Θ_{mis}	0.28	0.12	0.06	0.69	0.44	0.38	0.06	0.25	0.22	0.09	0.50	0.31	0.31
H_s	0.03	0.00	0.03	0.03	0.06	0.12	0.00	0.53	0.50	0.03	0.06	0.03	0.03
H_{max}	0.00	0.00	0.00	0.00	0.00	0.00	0.00	0.00	0.00	0.00	0.00	0.00	0.00
XH_{max}	0.00	0.00	0.00	0.00	0.00	0.00	0.00	0.00	0.00	0.00	0.00	0.00	0.00
T_p	0.06	0.00	0.00	0.25	0.25	0.44	0.00	0.53	0.53	0.12	0.19	0.38	0.38
Y_{wave}	0.00	0.00	0.00	0.00	0.00	0.00	0.00	0.00	0.00	0.00	0.00	0.00	0.00
$V_{current}$	0.00	0.00	0.00	0.00	0.00	0.00	0.00	0.00	0.00	0.06	0.00	0.00	0.00
$\Theta_{current}$	0.03	0.03	0.03	0.06	0.03	0.03	0.03	0.06	0.06	0.09	0.00	0.03	0.03
Cd_{upper}	0.00	0.00	0.00	0.00	0.00	0.00	0.00	0.00	0.00	0.00	0.00	0.00	0.00
Cd_{lower}	0.00	0.00	0.00	0.00	0.00	0.00	0.00	0.00	0.00	0.03	0.00	0.00	0.00
Cd_{axial}	0.00	0.00	0.00	0.00	0.00	0.00	0.00	0.00	0.00	0.00	0.00	0.00	0.00
$Cd_{rectangular}$	0.00	0.00	0.00	0.00	0.00	0.00	0.00	0.00	0.00	0.00	0.00	0.00	0.00

Appendix C: Fatigue calculation comparison

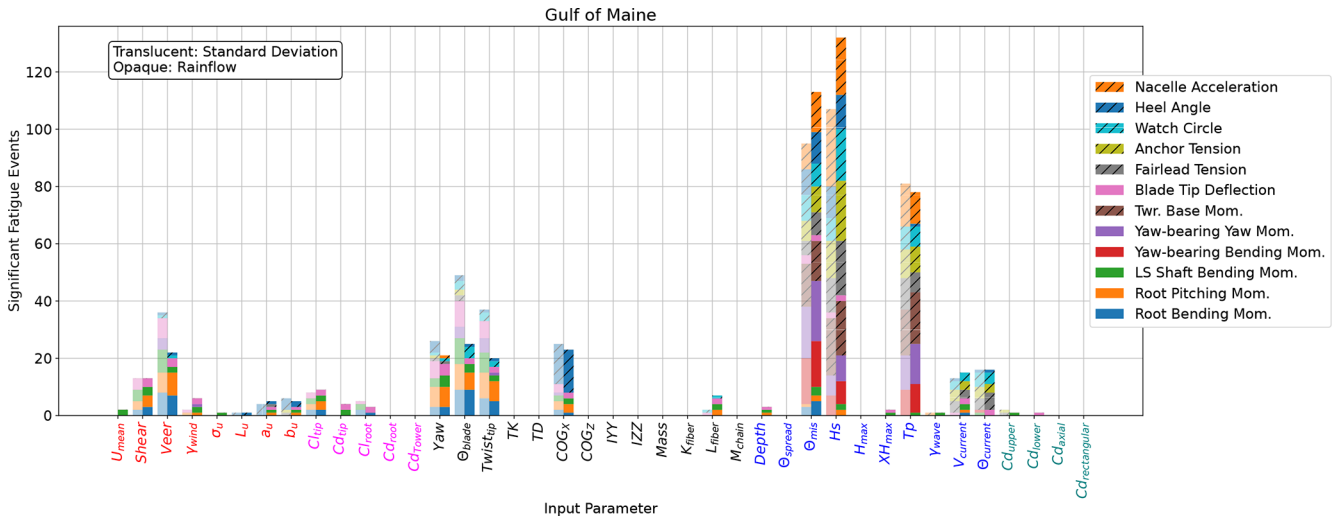


Figure C1. Sensitivity of fatigue load EE values for the IEA 15 MW RWT on the VolturUS-S platform in the Gulf of Maine when calculated with a rainflow counter and Miner’s rule compared to the standard deviation.

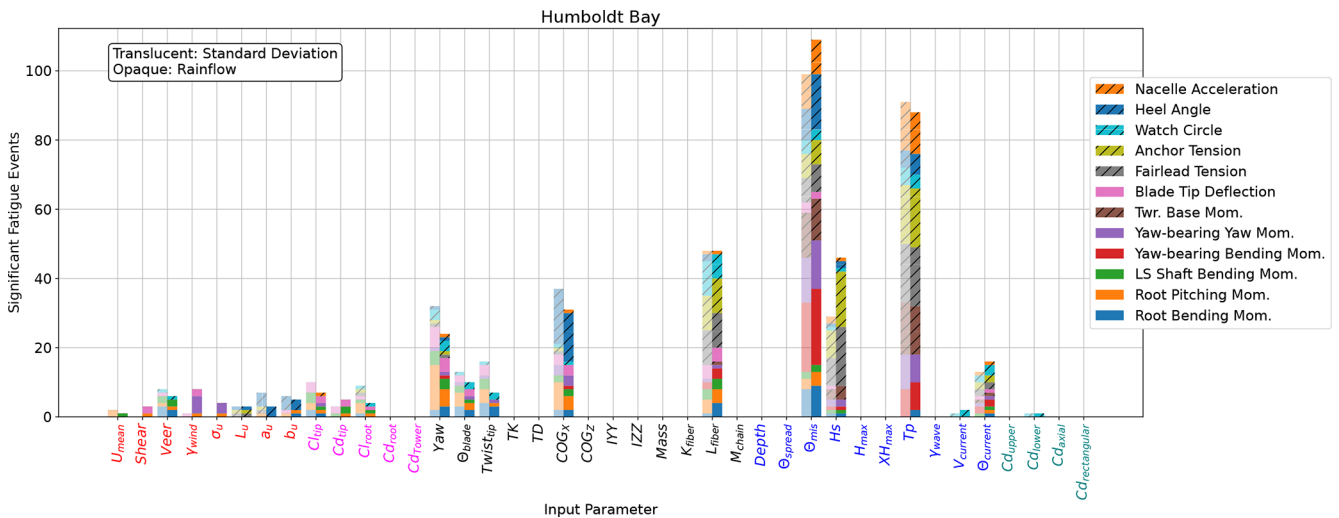


Figure C2. Sensitivity of fatigue load EE values for the IEA 15 MW RWT on the VolturUS-S platform in Humboldt Bay when calculated with a rainflow counter and Miner’s rule compared to the standard deviation.

Appendix D: Additional checks of seed convergence

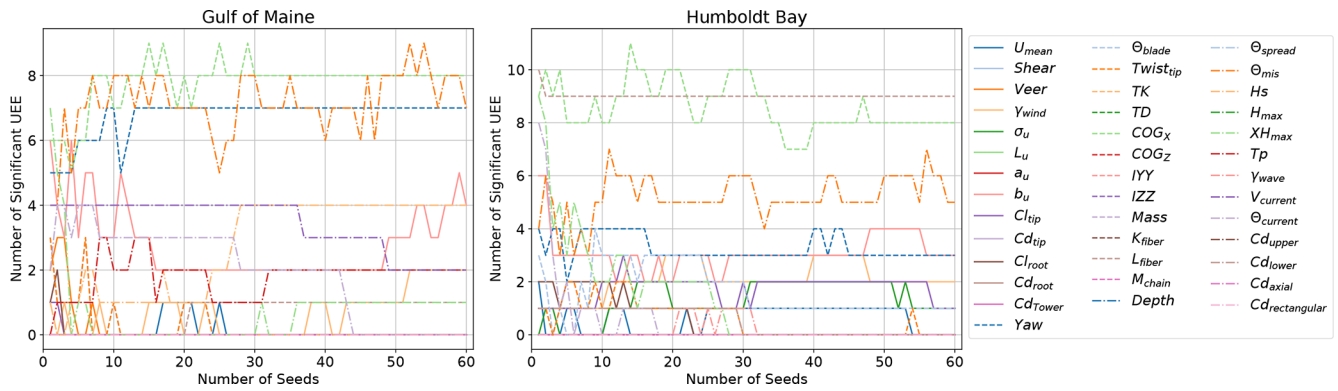


Figure D1. Convergence of ultimate load EE sensitivity for the IEA 15 MW RWT on the VoltturnUS-S platform with an increasing number of random seed numbers for one starting point only based on the nominal values for each input parameter.

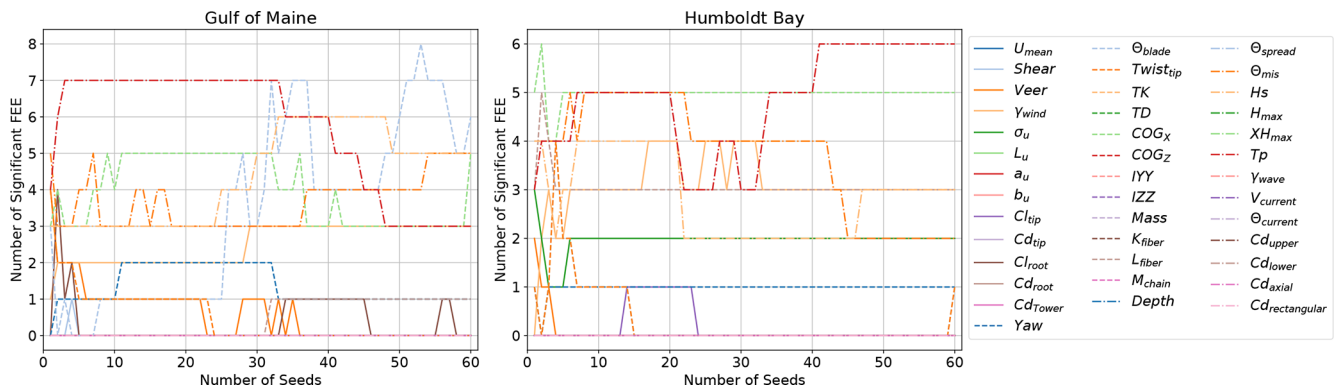


Figure D2. Convergence of fatigue load EE sensitivity for the IEA 15 MW RWT on the VoltturnUS-S platform with an increasing number of random seed numbers for one starting point only based on the nominal values for each input parameter.

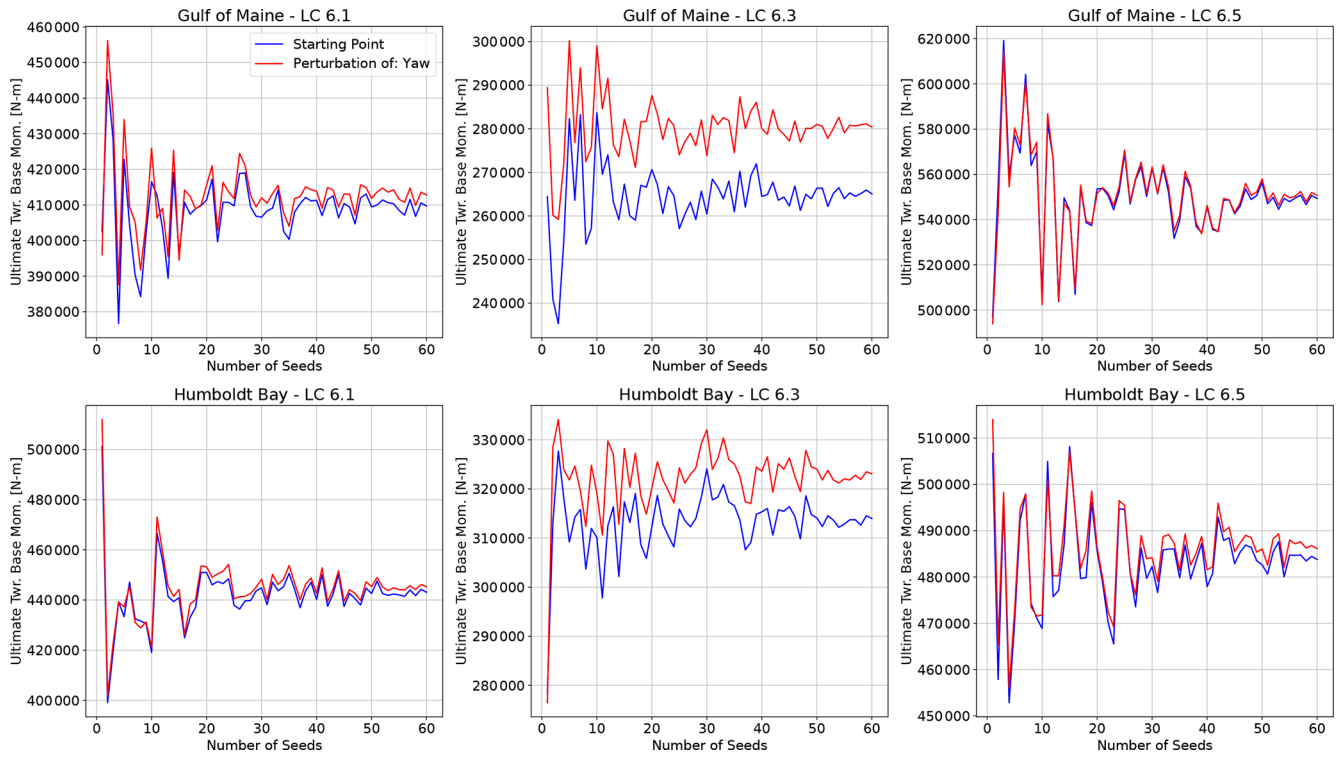


Figure D3. Seed convergence of the ultimate root pitching moment due to a change in the nacelle yaw (blue line: nominal starting point, red line: perturbation in yaw).

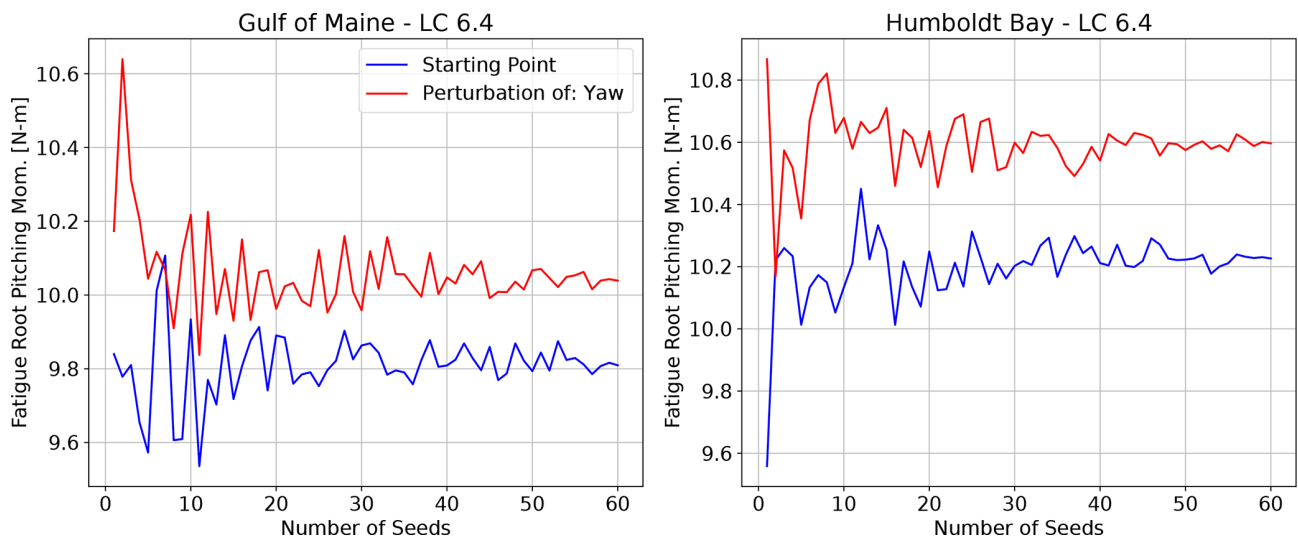


Figure D4. Seed convergence of the fatigue root pitching moment due to a change in the nacelle yaw (blue line: nominal starting point, red line: perturbation in yaw).

Code availability. The base OpenFAST input files and open-format versions of figures are publicly available on Zenodo at <https://doi.org/10.5281/zenodo.14933850> (Wiley et al., 2025).

Data availability. The wind data used in this project are publicly available through NREL (Bodini et al., 2023; <https://doi.org/10.2172/2274805>). The wave and current data used in this project are publicly available through NOAA (NOAA, 2024; <https://www.ndbc.noaa.gov/publications/>).

Author contributions. The project was conceptualized by JJ and AR, who provided coordination and direction of all aspects. The input parameter data processing and numerical model execution was performed by WW. The draft text was prepared by WW with editing and review from JJ and AR.

Competing interests. At least one of the (co-)authors is a member of the editorial board of *Wind Energy Science*. The peer-review process was guided by an independent editor, and the authors also have no other competing interests to declare.

Disclaimer. The views expressed in the article do not necessarily represent the views of the DOE or the U.S. Government.

Publisher's note: Copernicus Publications remains neutral with regard to jurisdictional claims made in the text, published maps, institutional affiliations, or any other geographical representation in this paper. While Copernicus Publications makes every effort to include appropriate place names, the final responsibility lies with the authors.

Special issue statement. This article is part of the special issue "NAWEA/WindTech 2024". It is a result of the NAWEA/WindTech 2024, New Brunswick, United States, 30 October–1 November 2024.

Acknowledgements. We would like to thank Lu Wang of NREL for performing the potential-flow calculations for the VoltumUS-S platform and Ericka Lozon and colleagues of NREL for providing the site-specific mooring systems used in this analysis (Lozon et al., 2025).

A portion of the research was performed using computational resources sponsored by the Department of Energy's Office of Energy Efficiency and Renewable Energy and located at NREL.

Financial support. Funding was provided by the U.S. Department of Energy Office of Energy Efficiency and Renewable Energy Wind Energy Technologies Office.

Review statement. This paper was edited by Alessandro Bianchini and reviewed by two anonymous referees.

References

- ABS: Selecting Design Wave by Long Term Stochastic Method, https://ww2.eagle.org/content/dam/eagle/rules-and-guides/current/offshore/238_Guidance_Notes_on_Selecting_Design_Wave_by_Long_Term_Stochastic_Method/Long_Term_Design_Wave_GN_e.pdf (last access: January 2024), 2016.
- Allen, C., Viselli, A., Dagher, H., Goupee, A., Gaertner, E., Abbas, N., Hall, M., and Barter, G.: Definition of the UMaine VoltumUS-S Reference Platform Developed for the IEA Wind 15-Megawatt Offshore Reference Wind Turbine, NREL/TP-5000-76773, <https://www.nrel.gov/docs/fy20osti/76773.pdf> (last access: January 2024), 2020.
- ArcGIS: Global Tidal Range, <https://www.arcgis.com/home/item.html?id=d5354dea41b14f0689860bf4b2cf5e8a> (last access: January 2024), 2024.
- Bangga, G., Carrion, M., Collier, W., and Parkinson, S.: Technical modeling challenges for large idling wind turbines, *J. Phys. Conf. Ser.*, 2626, 012026, <https://doi.org/10.1088/1742-6596/2626/1/012026>, 2023.
- Biglu, M., Hall, M., Lozon, E., and Housner, S.: Reference Site Conditions for Floating Wind Arrays in the United States, NREL/TP-5000-89897, <https://doi.org/10.7799/2425969>, 2024.
- Bodini, N., Redfern, S., Rybchuk, A., Pronk, V., Castagneri, S., Purkayastha, A., Draxl, C., Young, E., Roberts, B., Rosenlieb, E., Musial, W., Tai, S.-L., Berg, L., Rosencrans, D., Lundquist, J. K., and Optis, M.: NOW-23: The 2023 National Offshore Wind Data Set, NREL [data set], <https://doi.org/10.2172/2274805>, 2023.
- Bodini, N., Optis, M., Redfern, S., Rosencrans, D., Rybchuk, A., Lundquist, J. K., Pronk, V., Castagneri, S., Purkayastha, A., Draxl, C., Krishnamurthy, R., Young, E., Roberts, B., Rosenlieb, E., and Musial, W.: The 2023 National Offshore Wind data set (NOW-23), *Earth Syst. Sci. Data*, 16, 1965–2006, <https://doi.org/10.5194/essd-16-1965-2024>, 2024.
- Chetan, M. and Bortolotti, P.: Edgewise Structural Damping of a 2.8-MW Land-Based Wind Turbine Rotor Blade, *J. Phys. Conf. Ser.*, 2767, 022069, <https://doi.org/10.1088/1742-6596/2767/2/022069>, 2024.
- Cooperman, A., Duffy, P., Hall, M., Lozon, E., Shields, M., and Musial, W.: Assessment of Offshore Wind Energy Leasing Areas for Humboldt and Morro Bay Wind Energy Areas, California, NREL/TP-5000-82341, <https://www.nrel.gov/docs/fy22osti/82341.pdf> (last access: January 2024), 2022.
- Eckert-Gallup, A., Sallaberry, C., Dallman, A., and Neary, V.: Application of principal component analysis (PCA) and improved joint probability distributions to the inverse first-order reliability method (I-FORM) for predicting extreme sea states, *Ocean Eng.*, 112, 307–319, <https://doi.org/10.1016/j.oceaneng.2015.12.018>, 2016.
- Fowler, M., Lenfest, E., Viselli, A., Goupee, A., Kimball, R., Bergua, R., Wang, L., Zalkind, D., Wright, A., and Robertson, A.: Wind/Wave Testing of a 1:70-Scale Performance-Matched Model of the IEA Wind 15 MW Reference Wind Turbine with Real-Time ROSCO Control and Floating Feedback, *Machines*, 11, 865, <https://doi.org/10.3390/machines11090865>, 2023.

- Fuchs, R., Musial, W., Zuckerman, G., Chetan, M., Marquis, M., Rese, L., Cooperman, A., Duffy, P., Green, R., Beiter, P., Hernandez, D., Morris, J., Randall, A., Jossart, J., Mudd, L., and Vickery, P.: Assessment of Offshore Wind Energy Opportunities and Challenges in the U.S. Gulf of Mexico, NREL/TP-5000-88195, <https://www.nrel.gov/docs/fy24osti/88195.pdf> (last access: January 2024), 2023.
- Gaertner, E., Rinker, J., Sethuraman, L., Zahle, F., Anderson, B., Barter, G., Abbas, N., Meng, F., Bortolotti, P., Skrzypinski, W., Scott, G., Feil, R., Bredmose, H., Dykes, K., Shields, M., Allen, C., and Viselli, A.: Definition of the IEA Wind 15-Megawatt Offshore Reference Wind Turbine, NREL/TP-5000-75698, <https://www.nrel.gov/docs/fy20osti/75698.pdf> (last access: January 2024), 2020.
- IEC: Wind energy generation systems – Part 3-2: Design requirements for floating offshore wind turbines, International Electrotechnical Commission, IEC TS 61400-3-2, 2024.
- Klise, K., Pauly, R., Ruehl, K. M., Olson, S., Shippert, T., Morrell, Z., Bredin, S., Lansing, C., Macduff, M., Martin, T., Sivaraman, C., Gunawan, B., and Driscoll, F.: MHKiT (Marine and Hydrokinetic Toolkit) – Python, Zenodo [software], <https://doi.org/10.5281/zenodo.3924683>, 2020.
- Krieger, A., Ramachandran, G., Vita, L., Alonso, P., Almeida, G., Berque, J., and Aguirre, G.: LIFES50+: Qualification of innovative floating substructures for 10 MW wind turbines and water depths greater than 50 m, European Commission, <https://doi.org/10.3030/640741>, 2015.
- Krishnamurthy, R., García Medina, G., Gaudet, B., Gustafson Jr., W. I., Kassianov, E. I., Liu, J., Newsom, R. K., Sheridan, L. M., and Mahon, A. M.: Year-long buoy-based observations of the air–sea transition zone off the US west coast, *Earth Syst. Sci. Data*, 15, 5667–5699, <https://doi.org/10.5194/essd-15-5667-2023>, 2023.
- Lozon, E., Reddy Lekkala, M., Sirkis, L., and Hall, M.: Reference Mooring and Dynamic Cable Designs for Representative U.S. Floating Wind Farms, *Ocean Eng.*, 322, 120473, <https://doi.org/10.1016/j.oceaneng.2025.120473>, 2025.
- Morris, M.: Factorial Sampling Plans for Preliminary Computational Experiments, *Technometrics*, 33, 161–174, 1991.
- NOAA: National Data Buoy Center, <https://www.ndbc.noaa.gov/publications/> (last access: January 2024), 2024.
- NREL: OpenFAST, GitHub [code], <https://github.com/OpenFAST/openfast> (last access: September 2024), 2024.
- Petrone, G., Nicola, C., Quagliarella, D., Witteveen, J., and Iaccarino, G.: Wind Turbine Performance Analysis Under Uncertainty, in: AIAA Aerospace Sciences Meeting, Orlando, Florida, 4–7 January 2011, <https://doi.org/10.2514/6.2011-544>, 2011.
- Reddy, L., Karystinou, D., Milano, D., Walker, J., and Virè, A.: Influence of wind-wave characteristics on floating wind turbine loads: A sensitivity analysis across different floating concepts, *J. Phys. Conf. Ser.*, 2767, 062030, <https://doi.org/10.1088/1742-6596/2767/6/062030>, 2024.
- Robertson, A., Sethuraman, L., Jonkman, J., and Quick, J.: Assessment of Wind Parameter Sensitivity on Ultimate and Fatigue Wind Turbine Loads, NREL/CP-5000-70445, <https://www.nrel.gov/docs/fy18osti/70445.pdf> (last access: January 2023), 2018.
- Robertson, A. N., Shaler, K., Sethuraman, L., and Jonkman, J.: Sensitivity analysis of the effect of wind characteristics and turbine properties on wind turbine loads, *Wind Energ. Sci.*, 4, 479–513, <https://doi.org/10.5194/wes-4-479-2019>, 2019.
- Sanchez Gomez, M., Lundquist, J., Deskos, G., Arwade, R., Myers, A., and Hajjar, J.: Wind Fields in Category 1–3 Tropical Cyclones Are Not Fully Represented in Wind Turbine Design Standards, *J. Geophys. Res.*, 128, e2023JD039233, <https://doi.org/10.1029/2023JD039233>, 2023.
- Sandua-Fernandez, I., Vittori, F., Equinoa, I., and Cheng, P.: Impact of hydrodynamic drag coefficient uncertainty on 15 MW floating offshore wind turbine power and speed control, *J. Phys. Conf. Ser.*, 2362, 012037, <https://doi.org/10.1088/1742-6596/2362/1/012037>, 2022.
- Shaler, K., Robertson, A., Sethuraman, L., and Jonkman, J.: Assessment of Airfoil Property Sensitivity on Wind Turbine Extreme and Fatigue Loads, NREL/CP-5000-72892, <https://www.nrel.gov/docs/fy19osti/72892.pdf> (last access: January 2023), 2019.
- Shaler, K., Robertson, A. N., and Jonkman, J.: Sensitivity analysis of the effect of wind and wake characteristics on wind turbine loads in a small wind farm, *Wind Energ. Sci.*, 8, 25–40, <https://doi.org/10.5194/wes-8-25-2023>, 2023.
- Sobol, I.: On the distribution of points in a cube and the approximate evaluation of integrals, *USSR Computational Mathematics and Mathematical Physics*, 7, 86–112, 1967.
- Sørum, S., Katsikogiannis, G., Bachynski-Polić, E., Amdahl, J., Page, A., and Klinkvort, R.: Fatigue design sensitivities of large monopile offshore wind turbines, *Wind Energy*, 25, 1684–1709, <https://doi.org/10.1002/we.2755>, 2022.
- Vanem, E.: Uncertainties in extreme value modelling of wave data in a climate change perspective, *Journal of Ocean Engineering and Marine Energy*, 1, 339–359, <https://doi.org/10.1007/s40722-015-0025-3>, 2015.
- Venugopal, V., Varyani, K., and Westlake, P.: Drag and inertia coefficients for horizontally submerged rectangular cylinders in waves and currents, *P. I. Mech. Eng. M-J. Eng.*, 223, 121–136, <https://doi.org/10.1243/14750902JEME124>, 2008.
- Viselli, A., Faessler, N., and Filippelli, M.: Analysis of Wind Speed Shear and Turbulence LiDAR Measurements to Support Offshore Wind in the Northeast United States, in: Proceedings of the ASME 2018 1st International Offshore Wind Technical Conference. ASME 2018 1st International Offshore Wind Technical Conference, San Francisco, California, USA, 4–7 November 2018, V001T01A005, ASME, <https://doi.org/10.1115/IOWTC2018-1003>, 2018.
- Wiley, W., Jonkman, J., Robertson, A., and Shaler, K.: Sensitivity analysis of numerical modeling input parameters on floating offshore wind turbine loads, *Wind Energ. Sci.*, 8, 1575–1595, <https://doi.org/10.5194/wes-8-1575-2023>, 2023.
- Wiley, W., Jonkman, J., and Robertson, A.: File Sharing for: WES-2024-130 – Sensitivity analysis of numerical modeling input parameters on floating offshore wind turbine loads in extreme idling conditions, Zenodo [code], <https://doi.org/10.5281/zenodo.14933850>, 2025.